

Variability of hole spin qubits in planar Germanium

Biel Martinez^{1,*} and Yann-Michel Niquet^{2,†}

¹*Univ. Grenoble Alpes, CEA, LETI, F-38000, Grenoble, France*

²*Univ. Grenoble Alpes, CEA, IRIG-MEM-L_Sim, F-38000, Grenoble, France*

(Dated: July 8, 2025)

Hole spin qubits in Ge/GeSi heterostructures benefit from the clean environment of epitaxial interfaces and from the intrinsic spin-orbit coupling that enables efficient electrical control, which makes them promising candidates for quantum computation. However, spin-orbit coupling also enhances the sensitivity to electrical disorder, potentially increasing variability. In this work, we perform numerical simulations in a realistic device geometry to quantify the variability of the charge and spin properties of Ge qubits induced by charge traps at the SiGe/oxide interfaces. We show that while the variability of charge properties remains moderate, spin properties (g -factors and Rabi frequencies) show significant dispersion. We explore the implications of this variability for large-scale architectures, and provide guidelines to minimize variability both in terms of interface quality requirements and optimal operation strategies.

I. INTRODUCTION

Semiconductor spin qubits hold great promise for addressing the challenges of large-scale quantum computers [1, 2]. The electrical confinement of electrons and holes into quantum dots (QD) of nanometric size, and the use of their spin as a coherent carrier of information has been successfully demonstrated in a variety of materials including GaAs/AlGaAs [3, 4], Si/SiO₂ [5–8], Si/SiGe [9–11], and Ge/SiGe [12–16]. Interest has gradually focused on the last three materials because they can be isotopically purified from nuclear spins, thereby enhancing spin coherence [17–20]. In the past few years, high-fidelity single- [10, 21–23] and two-qubit gates [21–23] have been demonstrated in these platforms, as well as spin shuttling [24–26] and spin-photon coupling [27–29], the basic ingredients for quantum links between two-dimensional arrays [4, 14, 18, 30, 31]. This completes the toolkit needed to build large-scale spin qubit architectures [32–34].

Metal-oxide-semiconductor (MOS) spin qubits naturally benefit from the miniaturization and fabrication capabilities of classical microelectronics technologies [33, 35, 36]. However, the proximity with possibly charged amorphous materials and the defective nature of the Si/SiO₂ interface has been identified as a major source of qubit-to-qubit variability that could compromise scalability [37, 38]. In this context, epitaxial heterostructure devices have emerged as an alternative platform with a cleaner environment for the qubits, since the amorphous materials and defective interfaces are shifted a few tens of nanometers above the active layer [39–42]. Remarkable progress has been made recently in these heterostructures, with the demonstration of increasingly larger arrays of qubits [9, 12, 14, 16, 43–45]. In particular, hole spin qubits in Ge/GeSi heterostructures have become a compelling platform for quantum computing and simula-

tion [46, 47].

The intrinsic spin-orbit coupling (SOC) in hole spin qubits indeed enables the electrical manipulation of spins with radio-frequency electric fields [48] or spin shuttling [44] without the need for extrinsic elements such as micro-magnets. Nonetheless, SOC is a double-edge sword, as coupling the spins to electric fields opens the door to disorder-induced variability and extra dephasing channels. As for dephasing, the existence of sweet spots with enhanced coherence has been widely reported in hole spin qubits [15, 49–52]; yet qubit-to-qubit variability, while critical for holes in Si MOS devices [37], remains to be quantified for holes in Ge/SiGe heterostructures.

In this work, we quantify the variability of the charge and spin properties of hole spin qubits in Ge/GeSi heterostructures by means of numerical simulations on realistic, disordered devices. We introduce the devices and methodology in Section II, then quantify the variability of the charge and spin properties of the qubits in Section III, and finally discuss the implications for the operation of large-scale quantum processors in Section IV.

II. METHODOLOGY

We focus this variability study on the impact of charge traps on the charge and spin properties of Ge/SiGe QDs, for a prototypical device similar to Refs. [37, 50, 53, 54] (see Fig. 1a). This device emulates an unit cell of the two-dimensional array architecture of Refs. [16, 44]. We compute the variability induced by charge traps at the semiconductor/oxide interface. Such defects are believed to be the dominant source of variability in Si MOS spin qubits [37], and the cause of sizable energy fluctuations in Ge hole spin qubits [55]. We neglect other sources of variability such as dislocations or fabrication imperfections. We discuss the impact of residual long-range surface roughness [56] at the Ge/SiGe interfaces in Appendix A.

The simulated device is made of a 16 nm thick Ge well grown on a thick Ge_{0.8}Si_{0.2} buffer and covered with a 50

* biel.martinezidiaz@cea.fr

† yniquet@cea.fr

nm thick $\text{Ge}_{0.8}\text{Si}_{0.2}$ barrier. In each unit cell, a central gate C with a diameter of 100 nm confines the holes in a QD; and a set of four lateral gates (labelled L, R, T, B) controls the interactions between the QDs. They are grounded throughout this study, yet used to apply RF signals to drive the spin. The gates are 20 nm thick and are arranged in two layers: the L, R, T, B gates in a first layer on top of a 7 nm thick oxide (Al_2O_3), and the C gate in a second layer on top of a 14 nm thick oxide. The whole structure is encapsulated in 7 nm of Al_2O_3 . The simulation box contains 2×2 unit cells (with only the central dot occupied). The Ge well experiences a biaxial strain $\varepsilon_{xx} = \varepsilon_{yy} = \varepsilon_{\parallel} = -0.61\%$ and $\varepsilon_{zz} = \varepsilon_{\perp} = +0.45\%$ as a result of the lattice mismatch between Si and Ge, along with a residual in-plane strain $\varepsilon_{xx} = \varepsilon_{yy} = +0.26\%$ in the buffer [39]. Additionally, we include the inhomogeneous strains imprinted by the thermal contraction of the aluminium gates at cryogenic temperatures [54, 57, 58].

We randomly distribute point charges at the top $\text{Ge}_{0.8}\text{Si}_{0.2}/\text{Al}_2\text{O}_3$ interface to emulate dangling bonds of Si and Ge atoms, which we assume positively charged. We consider charge trap densities in the range $n_i = 10^{10} - 10^{12} \text{ cm}^{-2}$. The upper bound is the typical estimate for SiGe/oxide interfaces, while the lower bound highlights the gains in improving interface quality [59]. We solve Poisson's equation for the potential of these charges on a 3D mesh of the device, then a four-band Luttinger-Kohn Hamiltonian discretized with finite-differences on the same mesh. We obtain that way the single-hole ground-state energy ($E(1) = \mu$) and wave function in this potential (see Figs. 1b and 1c for an example). We also compute the charging energy as

$$U = E(2) - 2E(1), \quad (1)$$

using a full configuration interaction (CI) method [60, 61] for the two-particle ground-state energy $E(2)$. Finally, we make use of the g -matrix formalism [62] to calculate the spin properties of the qubit, namely the g -factors, Rabi frequencies (f_R) and dephasing times (T_2^*).

For each n_i , we collect statistics on 500 to 2500 simulations with independent, random realizations of the disorder. We apply the same gate voltage V_C for all realizations of a given n_i , and ground the other gates. We choose V_C so that the radius of the QD wave function is $r_{\parallel} = 28.3 \text{ nm}$ in a ‘‘pristine’’ device with a uniform charge distribution n_i that accounts for the average effect of the charge traps (equivalently $\ell_x = \ell_y = 20 \text{ nm}$, with $\ell_u = \sqrt{\langle u^2 \rangle - \langle u \rangle^2}$). The gate voltages are, therefore, $V_C = -53.7, -54.3, -55.4, -57.4, -63.4, -73.9, -96.3 \text{ mV}$ for $n_i = 10^{10}, 2.5 \times 10^{10}, 5 \times 10^{10}, 10^{11}, 2.5 \times 10^{11}, 5 \times 10^{11}, 10^{12} \text{ cm}^{-2}$, respectively. Note that larger gate potentials are needed to reach the same QD size for increasing n_i , as the traps ultimately rule the electrostatics of the QDs. The charging energy U of the pristine devices is $U \approx 2.4 \text{ meV}$ whatever n_i .

We then compute, for each relevant property f , its median \bar{f} , the Inter Quartile Range (IQR, hereafter labeled \mathcal{R}) and the relative Inter Quartile Range ($\tilde{\mathcal{R}}$) from the

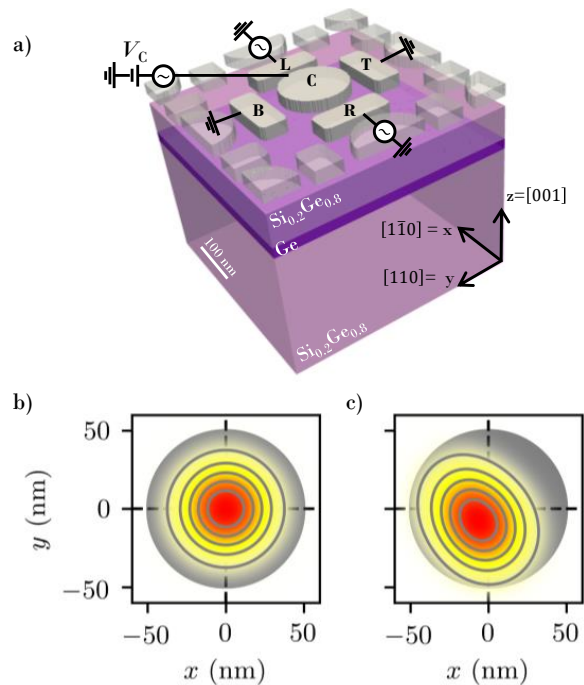


FIG. 1. a) Schematic representation of the simulated device. The active Ge layer is shown in purple, the top and bottom SiGe layers in pink, and the metallic gates in grey. The embedding oxide has been removed for clarity. b, c) Cross section of the ground-state density in the (xy) plane at the center of the Ge well for b) the pristine device and c) a defective device with $V_C = -57.4 \text{ mV}$ and $n_i = 10^{11} \text{ cm}^{-2}$. The shaded grey area highlights the position and dimensions of the C gate above.

percentiles (P) of the distribution as follows:

$$\bar{f} = P(50\%), \quad (2a)$$

$$\mathcal{R}(f) = P(75\%) - P(25\%), \quad (2b)$$

$$\tilde{\mathcal{R}}(f) = \mathcal{R}(f)/\bar{f}. \quad (2c)$$

We work with the median and IQR rather than the average and standard deviation as they are more robust and representative for non-normal distributions [63]. Moreover, we make use of a Bootstrap resampling method to assess the convergence of the statistics [64], and for each property we provide the 95% confidence intervals as error bars.

III. RESULTS AND DISCUSSION

In this Section we discuss the variability results. We focus on the variability of the charge properties in Subsection III A, and on the variability of the spin properties in Subsection III B.

A. Charge properties

To quantify the variability of the charge properties of Ge qubits, we monitor the chemical potential shift ($\Delta\mu$), the charging energy (U), the in-plane displacement (d_{\parallel}), and the in-plane size (r_{\parallel}) of the QDs. $\Delta\mu = \mu - \mu^0$ is the variation of the single-hole chemical potential μ induced by disorder, with μ^0 the chemical potential of the pristine device. The charging energy U is computed with CI, and the position and radius of the QD are defined as

$$d_{\parallel} = \sqrt{\langle x \rangle^2 + \langle y \rangle^2} \quad (3a)$$

$$r_{\parallel} = \sqrt{\langle x^2 \rangle + \langle y^2 \rangle - d_{\parallel}^2}, \quad (3b)$$

where $\langle x^n \rangle$ and $\langle y^n \rangle$ are the expectation values of x^n and y^n respectively.

In Fig. 2a we plot the histograms of the above charge properties for a trap density $n_i = 10^{11} \text{ cm}^{-2}$. $\Delta\mu$ shows fairly normal distributions, while U , d_{\parallel} and r_{\parallel} are slightly tailed (in part because they are positive quantities). The distribution of U 's mirrors the distribution of r_{\parallel} 's, as $U \propto 1/r_{\parallel}$ in a first approximation. All medians are in good agreement with the pristine device data at this n_i (orange line), except for d_{\parallel} (which can not be centered around zero because it is positive). The IQR of the distributions are plotted as a function of the trap density in Fig. 2b. The variability of the chemical potential reaches nearly 6 meV for $n_i = 10^{12} \text{ cm}^{-2}$. This is in line with previous estimations for double Ge QDs, and significantly better than for holes in Si MOS [55]. The absolute variability of the charging energies U is much smaller ($\mathcal{R}(U) \approx 925 \mu\text{eV}$ for $n_i = 10^{12} \text{ cm}^{-2}$). The operation of large-scale quantum processors would certainly benefit from $\mathcal{R}(\mu) \ll U$, as disorder would not compromise the occupancy of the qubits. Note that this regime is only accessible at low trap densities $n_i \lesssim 5 \times 10^{10} \text{ cm}^{-2}$. We discuss the impact of these results on the reliability of crossbar architectures in Section IV A.

The variations of the position and size of the disordered QDs remain moderate. The strong structural confinement along z yields to negligible fluctuations in $\langle z \rangle$ and ℓ_z (not shown). The vast majority of the QDs are well located under the C gate, even though a few ones undergo sizable displacements (13% of the devices move by $d_{\parallel} > 30 \text{ nm}$ at $n_i = 10^{11} \text{ cm}^{-2}$, the gate diameter being $d_C = 100 \text{ nm}$). The fluctuations of r_{\parallel} are also small, with $\mathcal{R}(r_{\parallel}) < 4 \text{ nm}$ whatever n_i . We provide in Fig. 1c a worst-case example of a deformed QD. These results show that charge disorder in the gate stack of Ge/SiGe heterostructures does not critically compromise the formation of the QDs, contrarily to what has been predicted for Si MOS devices [37]. This translates into a rather robust lever-arm $\alpha \approx 0.2$, with an IQR of only 0.04 for $n_i = 10^{12} \text{ cm}^{-2}$. The lever arm is not, therefore, a relevant metric to assess QD homogeneity in this system, as it is rather insensitive to the moderate fluctuations in QD position and size.

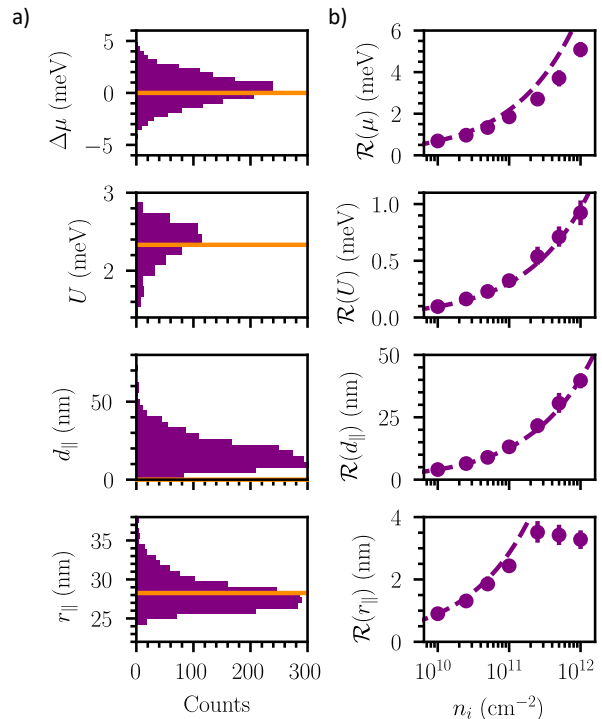


FIG. 2. Variability of the charge properties of Ge QDs in the device of Fig. 1a. a) Histogram of the chemical potential shifts $\Delta\mu$, the charging energy U , the in-plane displacements d_{\parallel} , and the in-plane radius r_{\parallel} of the QDs for a charge trap density $n_i = 10^{11} \text{ cm}^{-2}$ at $V_C = -57.4 \text{ mV}$. The horizontal orange lines are the values for the pristine device. b) Dependence of the IQR of $\Delta\mu$, U , d_{\parallel} , and r_{\parallel} on the charge trap density n_i . Dashed purple lines are guides to a $\propto \sqrt{n_i}$ dependence of the IQR.

The RSD of all charge properties shows the approximate $\propto \sqrt{n_i}$ behavior expected from perturbation theory [37], at least at low n_i . However, $\mathcal{R}(r_{\parallel})$ strikingly saturates when $n_i > 5 \times 10^{11} \text{ cm}^{-2}$. We remind that the calculations are made at the bias V_C such that $r_{\parallel} = r_{\parallel}^0 = 28.3 \text{ nm}$ in the pristine device with a uniform charge distribution at the SiGe/oxide interface. At low n_i , \bar{r}_{\parallel} is approximately equal to r_{\parallel}^0 , but when $n_i > 5 \times 10^{11} \text{ cm}^{-2}$, $\bar{r}_{\parallel} \lesssim r_{\parallel}^0$ (e.g., $\bar{r}_{\parallel} = 23.8 \text{ nm}$ at $n_i = 10^{12} \text{ cm}^{-2}$). The response to the stronger charge disorder indeed becomes non-linear and the median device is not the pristine device any more. The decrease of \bar{r}_{\parallel} and saturation of $\mathcal{R}(r_{\parallel})$ are fingerprints of these non-linearities, particularly prominent on these two quantities.

B. Spin properties

We next discuss the variability of the spin properties. We address the g -factors in Sec. III B 1, the Rabi frequencies in Sec. III B 2, and the dephasing times in Sec. III B 3.

1. g -factors

To calculate the Larmor frequencies $f_L = E_z/h$, we evaluate the g -matrix \hat{g} of each qubit from the wave functions at zero magnetic field [62]. The Zeeman splitting E_z then reads

$$E_z = \mu_B \sqrt{\mathbf{B}^T \hat{G} \mathbf{B}} = \mu_B g^* |\mathbf{B}|, \quad (4)$$

where μ_B is the Bohr magneton, \mathbf{B} is the magnetic field,

$$g^* = \sqrt{\mathbf{B}^T \hat{G} \mathbf{B}} / |\mathbf{B}| \quad (5)$$

is the effective g -factor, and

$$\hat{G} = \hat{g}^T \hat{g} \quad (6)$$

is the symmetric Zeeman tensor, which is an experimentally measurable quantity [65]. The eigenvalues of \hat{G} are the squares of the principal g -factors g_1 , g_2 and g_3 , and the eigenvectors of \hat{G} are the principal magnetic axes, which may not align with the device axes (the crystallographic x , y , z directions). We quantify this misalignment by two angles θ_g and φ_g . θ_g is the polar angle of the magnetic axis closest to z (the tilt of this magnetic axis with respect to z), while φ_g is the azimuthal angle of the magnetic axis closest to x (the angle between x and the in-plane projection of this magnetic axis, see Fig. 3).

We plot in Fig. 3 the median and IQR of the effective g -factor as a function of the magnetic field orientation, as well as the distribution of the angles θ_g and φ_g ($n_i = 10^{11} \text{ cm}^{-2}$). We also plot the distribution of the absolute difference $|g_1 - g_2|$ between the two principal ‘‘in-plane’’ g -factors (namely, those whose corresponding magnetic axes are closest to the plane).

As a consequence of disorder, the individual qubits may show anisotropic in-plane g -factors (Fig. 3g). Nevertheless, the median effective g -factor has the cylindrical symmetry. It matches the effective g -factor of the pristine device, reaching about 13.7 for out-of-plane and 0.13 for in-plane magnetic fields for all n_i (Figs. 3a-b). The dispersion of the g -factors, highlighted by the shaded area, results in the detuning of the Larmor frequencies of the qubits. We thus plot $\mathcal{R}(f_L)$ in Figs. 3c-d, at constant magnetic field amplitude $B = 1 \text{ T}$. $\mathcal{R}(f_L)$ shows a strong dependence on θ owing to the anisotropy of the g -factors. The absolute variability is maximal for $\mathbf{B} \parallel z$ [$\mathcal{R}(f_L, \mathbf{B} \parallel z) = 1172 \text{ MHz/T}$ while $\mathcal{R}(f_L, \mathbf{B} \parallel x) = 344 \text{ MHz/T}$]. However, the relative variability $\tilde{\mathcal{R}}(f_L) = \mathcal{R}(f_L)/\bar{f}_L$ is much larger in plane [$\tilde{\mathcal{R}}(f_L, \mathbf{B} \parallel z) = 6 \text{ MHz/GHz}$ and $\tilde{\mathcal{R}}(f_L, \mathbf{B} \parallel x) = 186 \text{ MHz/GHz}$]. This quantity actually characterizes the dispersion of the Larmor frequency when the amplitude of the magnetic field is adjusted so that the median Larmor frequency $\bar{f}_L \approx f_L^0$ is independent on the magnetic field orientation (with f_L^0 the Larmor frequency of the pristine device). It is, therefore, more relevant experimentally (as devices are usually tuned to operate at a target f_L). The IQR of the Larmor frequency at constant $f_L^0 = 2 \text{ GHz}$ is plotted in Figs.

3c and 3d. Therefore, in real *operando* conditions the variability of f_L is maximal for in-plane magnetic fields.

We next analyze the distribution of the angles θ_g and φ_g . Fig. 3e shows that one of the principal magnetic axes remains very close the growth direction $z = [001]$, $\bar{\theta}_g$ barely reaching 0.11° at $n_i = 10^{11} \text{ cm}^{-2}$ [66]. This small tilt essentially results from the inhomogeneous shear strains ε_{xz} and ε_{yz} imprinted by the differential contraction of the materials when the device is cooled down [54]. When d_{\parallel} is non-zero, the quantum dot experiences finite $\langle \varepsilon_{xz} \rangle$ and $\langle \varepsilon_{yz} \rangle$, which give rise to non-zero g -matrix elements g_{xz} and g_{yz} . The angle φ_g is much more distributed, which means that the in-plane axes are largely randomized by the disorder (see Fig. 3f). There are, nonetheless, two preferential orientations, $\varphi = 45^\circ$ [$\mathbf{x}' = (\mathbf{y} + \mathbf{x})/\sqrt{2}$], and $\varphi = -45^\circ$ [$\mathbf{y}' = (\mathbf{y} - \mathbf{x})/\sqrt{2}$]. This anisotropy is a fingerprint of the gates layout. Indeed, there are larger areas not covered by metal gates in these two directions. As a consequence, the traps in these areas are more weakly screened and give rise to stronger electric fields that tend to squeeze the dots along either \mathbf{x}' or \mathbf{y}' . The in-plane magnetic axes then align with the main axes of the resulting elliptical dot. As pointed out earlier, the principal g -factors of this elliptical dot are also different along the two in-plane axes. Noteworthy, the variability is slightly larger along \mathbf{x}' and \mathbf{y}' than along \mathbf{x} and \mathbf{y} (see Figs. 3b and 3d), even though \bar{g}^* is isotropic for in-plane magnetic fields. As shown in Ref. [50], the effective g -factors are indeed more responsive when the magnetic field is aligned with the main electric field fluctuations.

We finally plot the relative IQR $\tilde{\mathcal{R}}(g^*)$ as a function of n_i in Fig. 4a, for \mathbf{B} oriented along \mathbf{x} , \mathbf{y} and z . $\tilde{\mathcal{R}}(g^*)$ roughly scales as $\sqrt{n_i}$, as expected from perturbation theory [37]. $\tilde{\mathcal{R}}(g^*)$ shows by definition the same anisotropy as $\tilde{\mathcal{R}}(f_L)$. The relative variability of g_z^* is thus more than one order of magnitude smaller than the relative variability of g_x^* and g_y^* . Namely, $\tilde{\mathcal{R}}(g_z^*)$ remains below 1% while $\tilde{\mathcal{R}}(g_x^*)$ and $\tilde{\mathcal{R}}(g_y^*)$ range between 4 and 30% for trap densities from $n_i = 10^{10}$ to $n_i = 10^{12} \text{ cm}^{-2}$. Note that a large spread of the effective g -factors may compromise the individual addressability of the qubits in large-scale architectures. We discuss the implications in Sec. IV B.

Interestingly, the variations of g_x^* and g_y^* anti-correlate (Fig. 4b). We also observe clear correlations between g_x^* and $1/\ell_y^2$ (and between g_y^* and $1/\ell_x^2$). As a matter of fact,

$$\begin{aligned} g_x^* &= \sqrt{g_{xx}^2 + g_{yy}^2 + g_{zz}^2} \\ &= \sqrt{(3q + \delta g_{xx})^2 + \delta g_{yx}^2 + \delta g_{zx}^2} \end{aligned} \quad (7)$$

where $q = 0.06$ is the cubic Zeeman parameter and $\delta g_{\alpha\beta}$ are corrections due to confinement and strains, given by Eqs. (3) of Ref. [67]. When these corrections are small, $g_x^* \approx 3q + \delta g_{xx}$ is dominated by the variations of δg_{xx} . In homogeneous strains, the latter are $\delta g_{xx} \approx -a\langle p_y^2 \rangle + b\langle p_x^2 \rangle \propto -a/\ell_y^2 + b/\ell_x^2$ with $a \gg b$

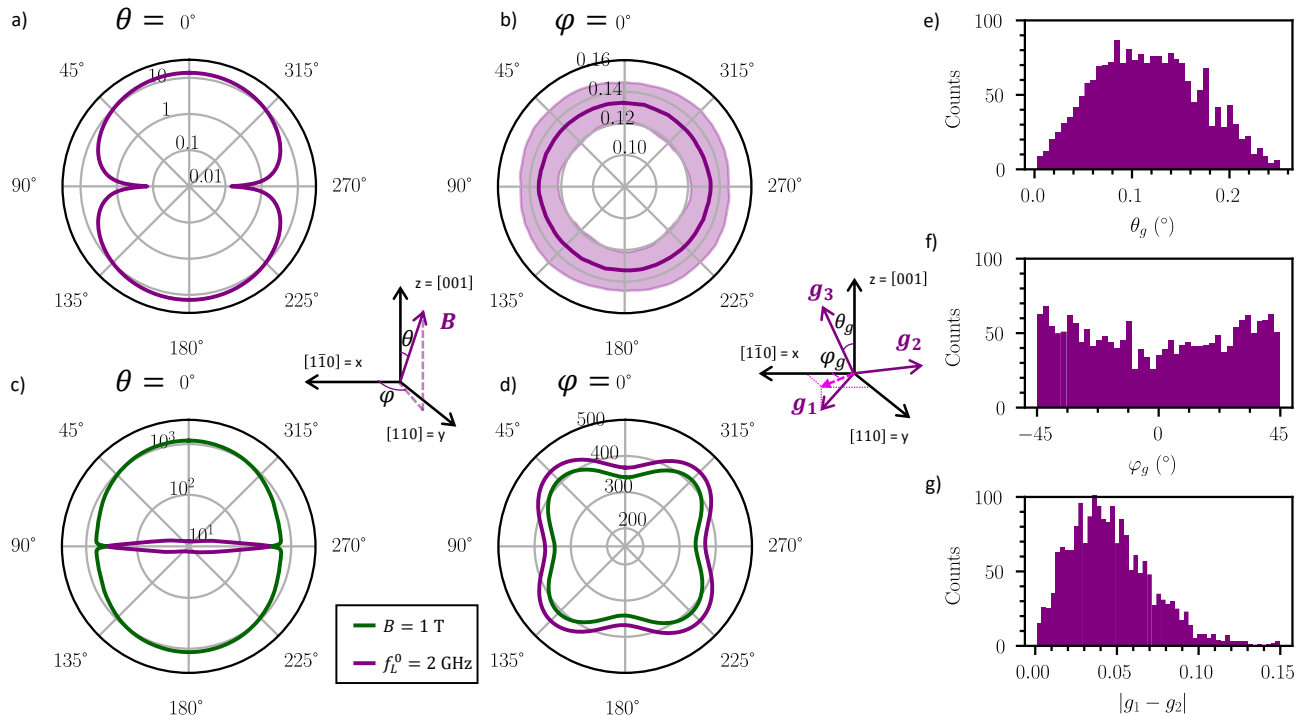


FIG. 3. Effective g -factor and magnetic axes variability for a charge trap density $n_i = 10^{11} \text{ cm}^{-2}$. a-b) Dependence of the effective g -factor on the angles θ and φ of the magnetic field $\mathbf{B} = B(\sin(\theta) \cos(\varphi), \sin(\theta) \sin(\varphi), \cos(\theta))$. The shaded areas is the inter-quartile range. c-d) Dependence of the IQR $\mathcal{R}(f_L)$ (in MHz) on the magnetic field orientation. The results are plotted at constant $B = 1 \text{ T}$ in green, and at the magnetic field amplitude such that $f_L = f_L^0 = 2 \text{ GHz}$ in the pristine device in purple. e-f) Distribution of θ_g and φ_g . g) Distribution of the difference $|g_1 - g_2|$ between the two principal in-plane g -factors. The insets define the angles θ and φ that characterize the orientation of the magnetic field, and the angles θ_g and φ_g that characterize the tilt of the magnetic axes.

(and p_x and p_y the momentum along x and y). Likewise, $g_y^* \approx 3q + \delta g_{yy}$ where $\delta g_{yy} \propto -a/\ell_x^2 + b/\ell_y^2$. We have also confirmed by calculations without cool-down strains (Appendix B) that the variability of the g -factors mainly results from the deformation of the dots rather than from their motion in the inhomogeneous strains, even though the latter are responsible for small rotations of the principal axes. As discussed in the next section, the inhomogeneous strains primarily give rise to a transverse coupling (Rabi oscillations) when the magnetic field goes in-plane.

All existing experiments on multiple Ge qubits show fingerprints of a significant variability of the effective g -factors. The four-qubit experiment of Ref. [14] reported $\bar{g}^* = 0.16, 0.24, 0.24, 0.26$ for an in-plane magnetic field. More recently, a Relative Standard Deviation (RSD) of 70% has been measured in a 10 QD device [44]. While this is considerably larger than predicted in Fig. 4a, in the experiment $\bar{g}^* = 0.04$ is much smaller than in the simulations (which may be a consequence of smaller or anisotropic QDs). In fact, the standard deviation of f_L is 392 MHz/T in the experiment, which is compatible with the data reported above for $n_i > 10^{11} \text{ cm}^{-2}$. In the same device but with a slightly off-plane magnetic field, $\bar{g}^* = 0.58$ and the RSD drops to 5% [16]. This is again

in line with the results shown here for $n_i \geq 10^{11} \text{ cm}^{-2}$. Finally, the variability of the principal axes and values of \hat{G} translates, at a given magnetic field orientation, in different precession axes for each qubit. This has also been observed in shuttling experiments [26], and recently exploited to perform one-qubit shuttling gates [44].

2. Rabi frequencies

In this section, we discuss the variability of the Rabi frequencies. Similar to previous studies [53, 54], we consider three kinds of resonant AC drives: with the plunger gate C ($V_C = V_{ac} \cos 2\pi f_L t$), with the left barrier gate L ($V_L = V_{ac} \cos 2\pi f_L t$), and with opposite modulations on the left and right barrier gates (L+R, $V_L = -V_R = \frac{1}{2} V_{ac} \cos 2\pi f_L t$). While the two first are commonly used in experiments [14, 16, 44], the L+R drive is interesting as it has the same symmetry as a homogeneous drive that displaces the QD as a whole (see Ref. [53] for details).

We compute the Rabi frequency f_R from the derivative \hat{g}' of the g -matrix with respect to the drive [62]:

$$f_R = \frac{\mu_B V_{ac}}{2\hbar |\hat{g}\mathbf{B}|} |\hat{g}\mathbf{B} \times \hat{g}'\mathbf{B}|, \quad (8)$$

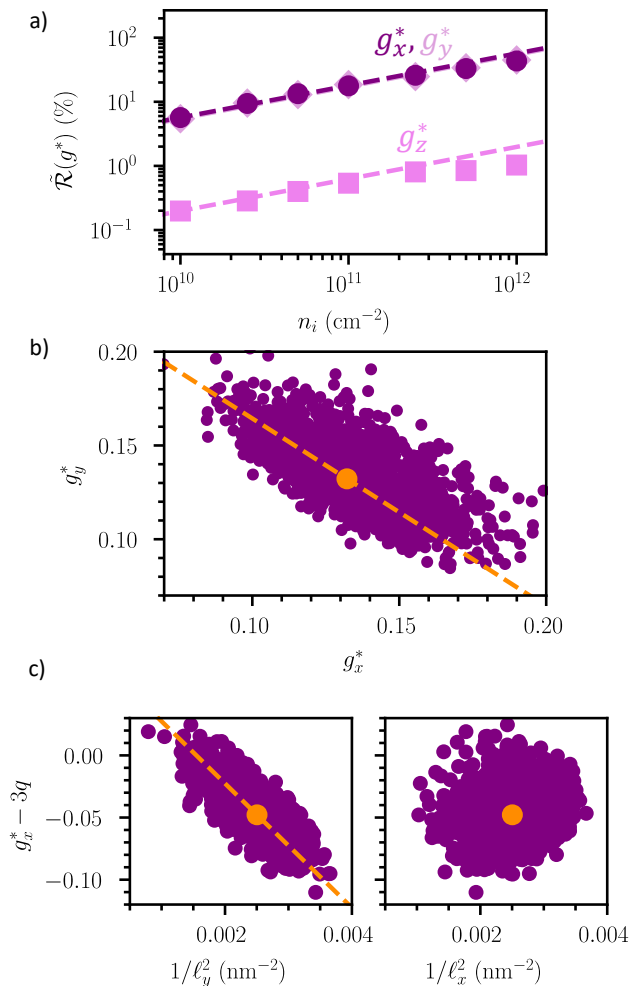


FIG. 4. Dependence of the relative IQR of the effective g -factors g_x^* , g_y^* and g_z^* on n_i . b) Correlation between the two in-plane g -factors g_x^* and g_y^* . The orange point is the data for the pristine device ($g_x^{*,0} = g_y^{*,0} = 0.13$), and the dashed orange line highlights an anti-correlation with slope -1 . c) Correlation between g_x^* and $1/\ell_y^2$, $1/\ell_x^2$. The orange point is the data for the pristine device, and the dashed orange line is a guide to the eye with slope -50 .

where V_{ac} is the amplitude of the drive, which we set to $V_{ac} = 1$ mV hereafter.

Recent studies have shown that the Rabi oscillations of hole spins in Ge can result from a wide variety of SOC mechanisms [53, 54]. The cubic Rashba SOI [68–70] characteristic of quasi-2D dots is rather weak at small vertical electric fields. The Rabi oscillations are, therefore, usually dominated by the modulations of the principal g -factors (“conventional” g -TMR) and principal axes of \hat{G} . The former result from the non-parabolic in-plane confinement and from the inhomogeneous vertical and drive fields, while the latter result from the coupling between the in-plane and out-of-plane motions of the hole [53], and from the motion in the inhomogeneous shear strains imprinted by the differential thermal contraction of the

materials [54]. They are particularly efficient when the magnetic field is near the heterostructure plane. The effects of strains may supersede the other mechanisms in the absence of disorder [54, 67]. The variability in position, shape and size of the QDs (Fig. 2), and in drive-induced displacements scatters the Rabi frequencies of the qubits.

Fig. 5 displays the median and IQR of the Rabi frequency as a function of the magnetic field angles θ (at $\varphi = 0^\circ$) and φ (at $\theta = 90^\circ$) for the different AC drives. The dataset contains 2000 realizations of disorder with a charge trap density $n_i = 10^{11}$ cm $^{-2}$, and has been computed at constant $f_L^0 = 2$ GHz (thus with an orientation-dependent magnetic field amplitude). We have added the pristine device data as the dashed orange lines for comparison.

There are significant differences between the median and pristine Rabi frequencies. When driving with the C gate, the QD breathes but does not move in-plane in the absence of disorder. Owing to the symmetry of the device, the average inhomogeneous shear strains experienced by the hole remain zero. The only SOC mechanism at work is thus the modulation of the main g -factors arising from the variations of the dot size (conventional g -TMR). In a perfectly circular QD, the two principal in-plane g -factors remain degenerate, and consequently the Rabi frequency vanishes for in-plane magnetic fields [71]. In the presence of disorder, however, the in-plane symmetry of the QD is broken, which enables conventional g -TMR for in-plane magnetic fields. Additionally, the dot is not necessarily centered under the gate, so that the C drive may displace the dot in the inhomogeneous strain field. The median Rabi frequency of the C gate is expected to be independent on φ . We find $\bar{f}_R/f_L^0 \approx 1$ MHz/mV/GHz at $\theta = 90^\circ$. However, \bar{f}_R rapidly decreases when θ goes out of plane due to the increase of g^* (thus the decrease of the magnetic field amplitude at constant $f_L^0 = 2$ GHz). The in-plane IQR is very large (see shaded area of Fig. 5a), as the disorder is responsible for the finite f_R . Variability significantly decreases when $\theta \geq 90^\circ$, which brings the optimal orientation slightly off-plane ($\theta \approx 87 - 89^\circ$ or $91 - 93^\circ$), where \bar{f}_R is roughly the same but the IQR is smaller than at $\theta \approx 90^\circ$. This is in line with the conclusions of Ref. [16], where the authors also identified off-plane magnetic fields as the optimal operation point. Note that Ref. [16] also showed that the C gate is more efficient in three-hole qubits.

For L and L+R drives, the angular dependence of the Rabi frequency is also smoothed out in the presence of traps, especially near the zeros of the Rabi frequency, which result from symmetry considerations (broken by the disorder) or from perfect cancellations between different mechanisms (also blurred by disorder). The median Rabi frequencies are slightly smaller than in the pristine device and reach $\bar{f}_R/f_L^0 \approx 5$ MHz/mV/GHz for $\mathbf{B} \parallel \mathbf{x}$ ($\theta = 90^\circ$, $\varphi = 0^\circ$). The IQR is also maximal in plane, and is weakly dependent of φ ($\mathcal{R}(f_R)/\bar{f}_L \approx$

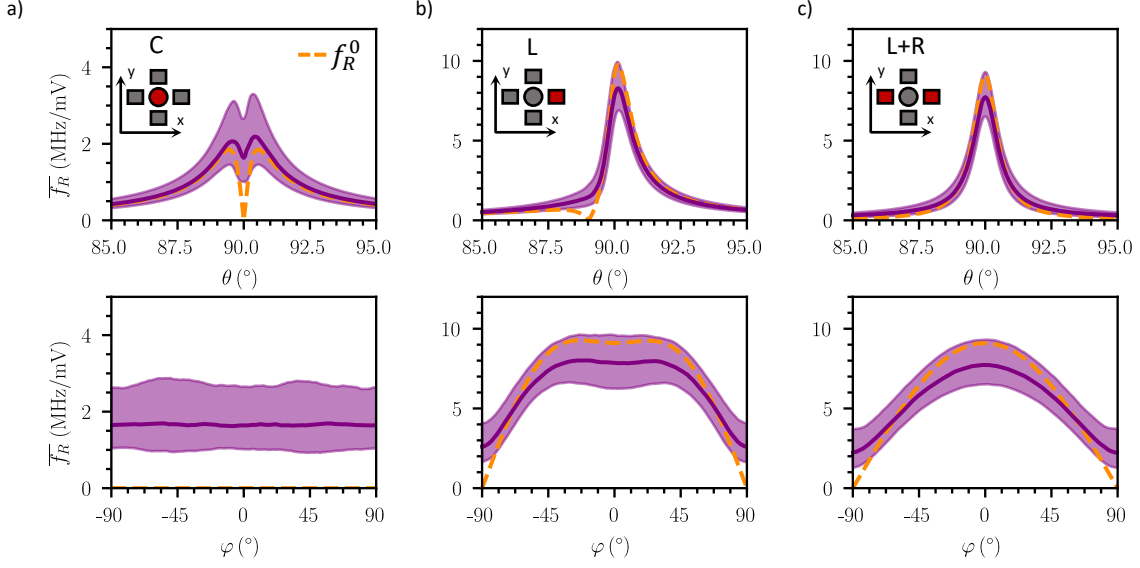


FIG. 5. Rabi frequency anisotropy in pristine and disordered devices. a) Median Rabi frequency as a function of θ (for $\varphi = 0^\circ$) and φ (for $\theta = 90^\circ$) when driving with the C gate, for defective devices with trap density $n_i = 10^{11} \text{ cm}^{-2}$. The magnetic field amplitude is varied so that the Larmor frequency is $f_L^0 = 2 \text{ GHz}$ in the pristine device whatever the orientation. The dashed orange line is the Rabi frequency of the pristine device, and the shaded purple areas highlight the IQRs. b) Same for the L drive. c) Same for the L+R drive.

1.7 MHz/mV/GHz at $n_i = 10^{11} \text{ cm}^{-2}$). The optimal magnetic field orientation for the L and L+R drives is $\theta \rightarrow 90^\circ$ and $\varphi \rightarrow 0^\circ$ where f_R is maximal.

In order to disclose the dominant driving mechanism, we split the total f_R into different contributions. We first diagonalize the g -matrix $\hat{g} = \text{diag}(g_1, g_2, g_3)$ of each qubit by choosing an appropriate spin basis set and the principal axes for the magnetic field coordinates [62]. We next split the \hat{g}' -matrix in this representation into three blocks:

$$\hat{g}'_{\text{TMR}} = \begin{bmatrix} g'_{11} & 0 & 0 \\ 0 & g'_{22} & 0 \\ 0 & 0 & g'_{33} \end{bmatrix}, \quad (9a)$$

$$\hat{g}'_{\theta_g} = \begin{bmatrix} 0 & 0 & g'_{13} \\ 0 & 0 & g'_{23} \\ g'_{31} & g'_{32} & 0 \end{bmatrix}, \quad (9b)$$

$$\hat{g}'_{\varphi_g} = \begin{bmatrix} 0 & g'_{12} & 0 \\ g'_{21} & 0 & 0 \\ 0 & 0 & 0 \end{bmatrix}. \quad (9c)$$

The first one, \hat{g}'_{TMR} , is the conventional g -TMR resulting from the electrical modulations of the principal g -factors. The second one, \hat{g}'_{θ_g} , collects the off-diagonal elements g'_{13} , g'_{31} , g'_{23} and g'_{32} that primarily capture the variations of the tilt θ_g of the out-of-plane principal axis (and the Rashba SOI) [53, 54]. The third one, \hat{g}'_{φ_g} , essentially accounts for the variations of the orientation φ_g of the in-plane principal axes. The total \hat{g}' matrix is therefore $\hat{g}' = \hat{g}'_{\text{TMR}} + \hat{g}'_{\theta_g} + \hat{g}'_{\varphi_g}$. We can thus compute $\mathbf{f}_{R,\alpha}$ and $f_{R,\alpha} =$

$|\mathbf{f}_{R,\alpha}|$ using \hat{g}'_α in Eq. (8) for $\alpha \in [\text{TMR}, \theta_g, \varphi_g]$. Note that the individual contributions can make constructive or destructive interferences as $f_R = |\mathbf{f}_{R,\text{TMR}} + \mathbf{f}_{R,\theta_g} + \mathbf{f}_{R,\varphi_g}|$.

We plot in Fig. 6a the correlation between f_R and f_{R,θ_g} for the C drive and $\mathbf{B} \parallel \mathbf{x}$. The modulations of θ_g resulting from the motion in the inhomogeneous shear strains make the main contribution to f_R for in-plane magnetic fields. Yet $f_R < f_{R,\theta_g}$ for several devices because the interference between the shear strains and the other mechanisms is usually destructive for the C drive.

For L and L+R drives, the Rabi oscillations are clearly ruled by \hat{g}'_{θ_g} , and, more specifically, by the large g'_{13} resulting from the motion of the dot in the inhomogeneous shear strains (see Figs. 6b and 6c, where f_{R,θ_g} and f_R show a remarkable correlation with slope 1). \bar{f}_R is maximal at $\theta = 90^\circ$, and shows an approximate $\cos(\varphi)$ dependence for in-plane magnetic fields, another fingerprint of the dominant g'_{13} . Therefore, the electrical modulation of θ_g by strain is still the prevalent driving mechanism when the QD is shaken in a disordered potential. Moreover, \mathbf{f}_{R,θ_g} is mostly orthogonal to $\mathbf{f}_{R,\text{TMR}}$ and \mathbf{f}_{R,φ_g} , which tend to be antiparallel and cancel each other.

We plot in Fig. 6 the median $\bar{f}_{R,x}$ and the relative IQR $\tilde{\mathcal{R}}(f_{R,x})$ of the Rabi frequency for $\mathbf{B} \parallel \mathbf{x}$ as a function of the trap density. The variability of the C drive is the largest (around 100% whatever n_i). This results from the fact that the Rabi oscillations are promoted by disorder ($\bar{f}_{R,x}$ and $\sigma(f_{R,x}) \rightarrow 0$ when $n_i \rightarrow 0$). The L and L+R drives show similar variabilities, ranging from 90%

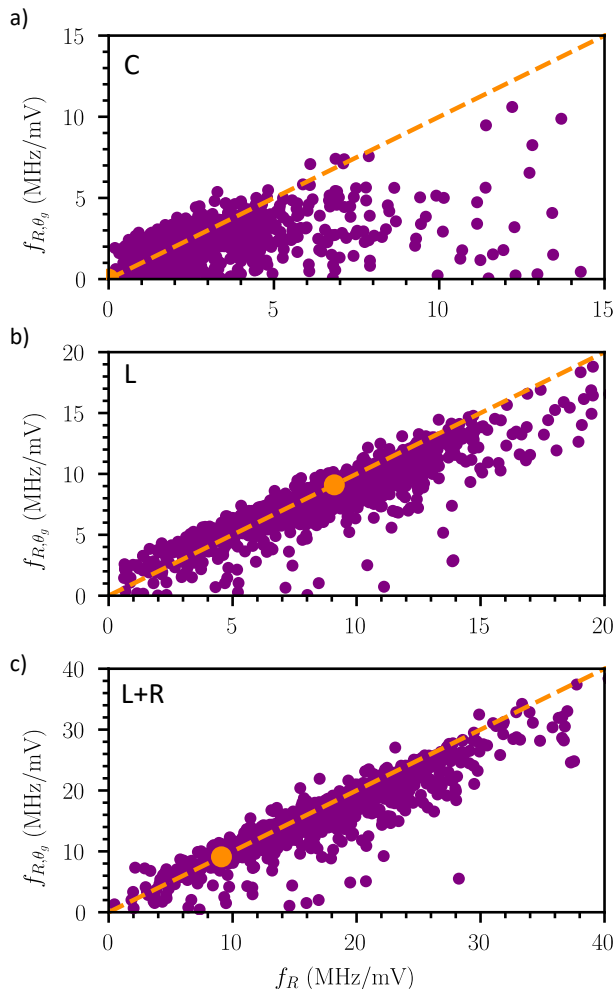


FIG. 6. Mechanisms of the Rabi oscillations. a-c) Correlations between the Rabi frequency f_R of the disordered devices and the contribution f_{R,θ_g} from the modulations of θ_g , for the C, L, and L+R drives. This contribution primarily results from the motion of the hole in the inhomogeneous shear strains. The magnetic field is oriented along $\theta = 90^\circ$ and $\varphi = 0^\circ$ ($\mathbf{B} \parallel \mathbf{x}$), and its amplitude is chosen so that $f_L^0 = 2$ GHz. The orange point is the pristine device data, and the dashed orange line is a guide-to-the-eye for $f_{R,\theta_g} = f_R$.

for $n_i = 10^{12} \text{ cm}^{-2}$ down to 10% for $n_i = 10^{10} \text{ cm}^{-2}$. At variance with the C drive, $\bar{f}_{R,x}$ is weakly dependent on n_i and $\tilde{\mathcal{R}}(f_{R,x})$ follows the $\propto \sqrt{n_i}$ dependence expected from first-order perturbation theory [37]. These results emphasize that the side gates achieve both larger Rabi frequencies and lower variability (for single holes). Surprisingly, these levels of variability are not much smaller than reported for Si MOS despite the lower disorder in the vicinity of the qubits [37]. It is nonetheless worth noting that inhomogeneous strains are not accounted for in Ref. [37], but appear to be the main driving mechanisms here.

The Rabi frequencies reported above are consistent

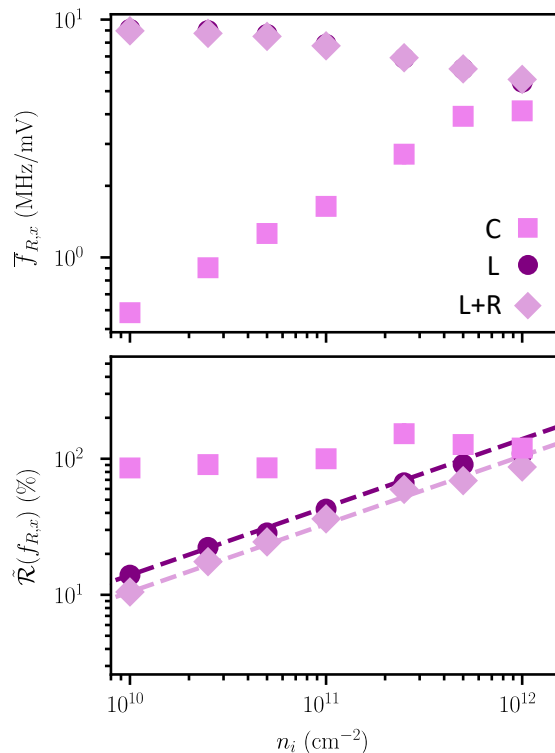


FIG. 7. a) Median Rabi frequency \bar{f}_R and b) relative IQR $\tilde{\mathcal{R}}(f_R)$ as a function of n_i when driving with the C gate (squares), L gate (circles) and L+R gates (diamonds). The magnetic field is oriented along $\theta = 90^\circ$ and $\varphi = 0^\circ$ ($\mathbf{B} \parallel \mathbf{x}$), and its amplitude is chosen so that $f_L^0 = 2$ GHz. The dashed lines highlight the $\tilde{\mathcal{R}}(f_R) \propto \sqrt{n_i}$ dependence expected from first-order perturbation theory.

with previous simulation studies using similar geometries [50, 54] and with the existing experimental data. In Ref. [14], $\bar{f}_R/\bar{f}_L = 5.5 \text{ MHz/mV/GHz}$ for in-plane magnetic fields and drives equivalent to L. In the 10 qubits experiment of Ref. [16], the authors systematically characterized f_R for the C and L drives. For $\theta \approx 87^\circ$ and $\varphi \approx 45^\circ$, they measure $\bar{f}_R/\bar{f}_L = 0.14 \text{ MHz/mV/GHz}$ and 0.18 MHz/mV/GHz for the C and L drive, respectively. Additionally, the relative IQR reaches roughly 50% for both drives. These results are qualitatively compatible with those reported here for $n_i \geq 10^{11} \text{ cm}^{-2}$.

3. Dephasing

We next study the anisotropy of charge-noise-driven dephasing in the presence of static disorder. We emphasize that the defects responsible for charge noise and for variability are in principle different. On the one hand, variability is due to deep traps at the SiGe/oxide interface that rarely undergo trapping/detrapping events. On the other hand, dephasing is due to shallower traps whose state switches during the experiment (e.g., through

charge transfers between the traps and the gates above or charge hopping between neighboring traps). The electric field generated by these two-level fluctuators (TLFs) modulates the vertical and in-plane confinement of the quantum dot, as do the gates. In a first approximation, we can therefore lump the effects of the TLFs into effective gate voltage modulations (provided the gates sample a relevant set of electrical perturbations), and estimate the dephasing rate as [50, 52]

$$\Gamma_2^* = \frac{1}{T_2^*} = \sqrt{2\pi} \sqrt{\sum_{\alpha} [\delta V_{\alpha}^{\text{rms}} \text{LSES}(\alpha)]^2}, \quad (10)$$

where $\alpha \in [\text{C}, \text{L}, \text{R}, \text{B}, \text{T}]$ [72], V_{α}^{rms} is the rms amplitude of the noise on gate α , and

$$\text{LSES}(\alpha) = \frac{\partial f_L}{\partial V_{\alpha}} \quad (11)$$

is the longitudinal spin electric susceptibility [49, 52]. In this study, we set $V_{\alpha}^{\text{rms}} = 10 \mu\text{eV}$ for all gates, which yields values of Γ_2^* that are consistent with experiments. Note that this simple model relies on quite strong assumptions, as it can only capture the effect of TLFs that are close to the gates, but may fail to describe the effect of TLFs located between the gates. The general trends discussed below are not, however, expected to be dependent on the details of the model. We discuss the limitations of this model in more details hereafter.

We compute the LSES and estimate Γ_2^* with Eq. (10) for each defective device, and plot the median dephasing rate $\bar{\Gamma}_2^*$ and IQR $\mathcal{R}(\Gamma_2^*)$ in Fig. 8.

In the absence of disorder, Γ_2^* is minimal for $\theta = 0^\circ$ and maximal for $\theta = 90^\circ$ as the in-plane g -factors are more sensitive to noise [50]. Γ_2^* exhibits, nevertheless, local optimums for in-plane magnetic fields at $\varphi = \pm 45^\circ$. The median dephasing rate $\bar{\Gamma}_2^*$ of the disordered devices shows the same anisotropy. As discussed in Section III B 2, the Rabi frequency is sizable only when $\theta \approx 90^\circ$, so that the domains $\theta \rightarrow 0^\circ$ and $\theta \rightarrow 180^\circ$ where $\bar{\Gamma}_2^*$ decreases drastically are hardly exploitable experimentally. We discuss this matter in more details in Section IV C. With $V_{\alpha}^{\text{rms}} = 10 \mu\text{eV}$, $\bar{\Gamma}_2^*$ reaches $\approx 1 \text{ MHz}$ for $\theta = 90^\circ$ and $\varphi = 0^\circ$. We emphasize that the two in-plane minima at $\varphi = \pm 45^\circ$ are highly dependent on the TLFs model. They result in the present description from the fact that the gates hardly capture the effects of electric field fluctuations along the diagonals of the device (the [100] and [010] axes). The electric field noise shall actually be stronger along $x = [1\bar{1}0]$ and $y = [110]$ if the traps exchange charges with the gates (as only traps below the gates can then switch). This assumption breaks down, however, if hopping or reconfiguration of traps between the gates play a major role (especially because they are not screened by the gates). The contrast between the in-plane extrema of $\bar{\Gamma}_2^*$ along [100]/[010] and along [1 $\bar{1}$ 0]/[110] is thus highly dependent on the nature and distribution of the traps (largely unknown at this stage), but the overall dependence on θ is expected to be solid.

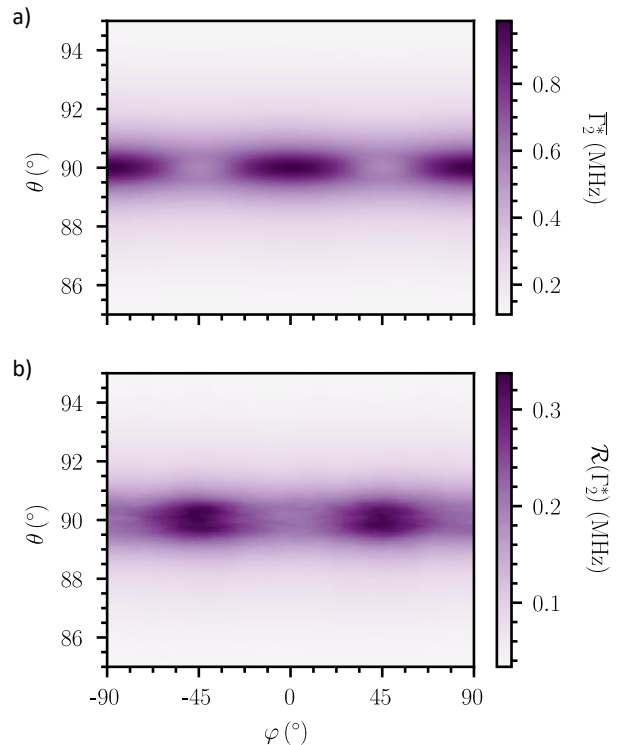


FIG. 8. Dephasing in the presence of disorder. (a) Median and (b) IQR of the dephasing rate Γ_2^* as a function of the magnetic field orientation for $n_i = 10^{11} \text{ cm}^{-2}$. The amplitude of the magnetic field is chosen so that $f_L^0 = 2 \text{ GHz}$.

The IQR of Γ_2^* is also maximal in-plane at $\varphi = \pm 45^\circ$, and minimal at $\varphi = 0^\circ$. This dependence is, again, a fingerprint of the gate layout and model for charge noise.

In Fig. 9 we plot $\bar{\Gamma}_2^*$ as a function of n_i at $\theta = 90^\circ$, $\varphi = 45^\circ$, as well as the IQR (shaded purple area), the value in the pristine device, and the maximal Γ_2^* among the 95% best devices. $\bar{\Gamma}_2^*$ shows a sizable increase with n_i , which is not observed for the pristine device. The IQR of Γ_2^* also increases significantly, and reaches $\mathcal{R}(\Gamma_2^*) = 0.9 \text{ MHz}$ at $n_i = 10^{12} \text{ cm}^{-2}$. These two observations are in fact tightly related: as Γ_2^* is positive by definition, but the LSES in Eq. (10) are signed, a large variability of the latter yields to an increase of both the median and IQR of the former. Finally, $\max(\Gamma_2^*)$ also illustrates the tailed nature of the distribution of Γ_2^* . As defined here, $\max(\Gamma_2^*)$ is nothing else than the 95th percentile, and is significantly larger than the value $1.22\mathcal{R}(\Gamma_2^*)$ expected for normal distributions. It is a relevant metric because the performance of a large scale quantum processor are limited by the qubits with fastest decoherence. We explore the constraints that this implies in Section IV C.

In the appendices, we provide additional data on the dependence of the variability on V_C (the confinement strength, Appendix C), and on the top GeSi barrier thickness H_{SiGe} (Appendix D). We show, as expected, that

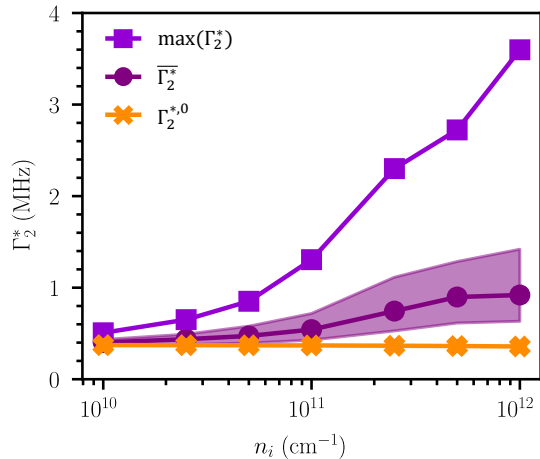


FIG. 9. Dependence of Γ_2^* on n_i . $\bar{\Gamma}_2^*$ is plotted with purple dots, with the IQR highlighted by the shaded area. The pristine device value ($\Gamma_2^{*,0}$) is plotted with orange crosses, and the maximum Γ_2^* among the 95% best devices with violet squares. The magnetic field is oriented along $\theta = 90^\circ$, $\varphi = 45^\circ$, and its amplitude is chosen so that $f_L^0 = 2$ GHz.

increasing H_{SiGe} (thus bringing the traps farther away from the Ge well) reduces variability.

IV. IMPLICATIONS OF VARIABILITY FOR ARRAYS OF SPIN QUBITS

In this Section we discuss the implications of the results discussed above on the performance of large-scale spin qubit architectures. In Subsection IV A we discuss how the variability in μ can compromise the functionality of crossbar architectures. In Subsection IV B, we address the constraints on single-qubit addressability imposed by the variability in g^* . Finally, in Subsection IV C we explore how the variability in f_R and Γ_2^* can compromise the performance of a large-scale quantum processor.

A. Crossbar architectures

Spin qubit platforms will inevitably face routing challenges as they scale up. These challenges are more difficult to tackle when the pitch is small and the number of control knobs per qubit is large. One proposed strategy to address this problem is to implement shared control schemes, such as the so-called crossbar architectures [32, 33, 73]. A 4×4 crossbar array has actually been fabricated and characterized in Ge/SiGe heterostructures, and odd charge occupancy achieved in all QDs [30].

In crossbar architectures, several qubits generally share the same gate potential. It is clear, therefore, that disorder-induced variations of the chemical potential μ can impede the operation of the devices. In particular,

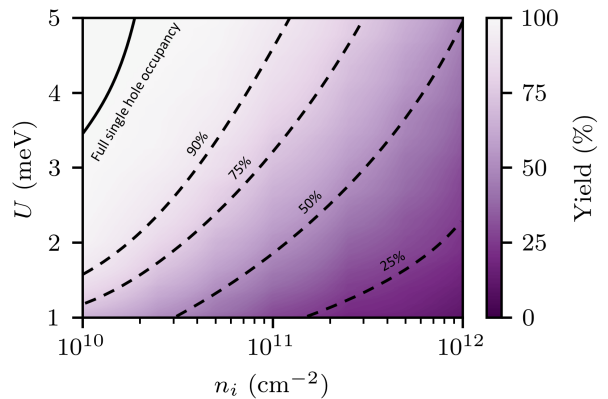


FIG. 10. Fraction of devices fulfilling $|\Delta\mu| < U/2$ as a function of the charging energy U and trap density n_i .

single-hole occupancy can be compromised in the qubits whose $|\Delta\mu|$ is larger than $U/2$. As a matter of fact, not all QDs could be biased in the single-hole regime in the crossbar array of Ref. [30]. A key condition for reliable crossbar operation is thus $|\Delta\mu| < U/2$ for all qubits.

$\mathcal{R}(\mu)$ and $\mathcal{R}(U)$ are plotted as a function of n_i in Fig. 2. As discussed before, $\mathcal{R}(U)$ is much smaller than $\mathcal{R}(\mu)$. Therefore, we consider hereafter U as a deterministic parameter that defines the margins of operation. We monitor the fraction of devices that fulfill $|\Delta\mu| < U/2$ in the datasets of Fig. 2b, and plot this yield as a function of n_i and U in Fig. 10 [74].

Single hole occupancy can always be achieved in $> 90\%$ of the devices for large enough U . However, the median charging energy of the present QDs is only $\bar{U} \approx 2.4$ meV. Reaching such yields for $U < 2.5$ meV actually demands very good interface qualities $n_i \lesssim 3 \times 10^{10} \text{ cm}^{-2}$. We achieve full single hole occupancy in the sets of 1000 to 2500 simulated devices only for $U > 3.5$ meV when $n_i \rightarrow 10^{10} \text{ cm}^{-2}$, which is at the state-of-the-art of micro-electronics technologies (yet for Si/SiO₂, not for SiGe/Al₂O₃ interfaces) [75–78]. We emphasize, though, that the “full single hole occupancy” line on Fig. 10 is indicative and not statistically meaningful (as outliers can still appear in different or larger samples of devices). These results show that crossbar architectures may indeed suffer from the variability in μ , and that reliable functionality would require large U and/or a substantial improvement in interface quality. Alternatively, specific gate layouts have been proposed to cope with the variability in μ , and could ease the implementation of such architectures [55].

B. Individual qubit addressability

Another challenge for scalability is qubit addressability. In arrays of spin qubits, one-qubit gates may rely on the dependence of f_L on the electrical confinement (the

Stark shift) to bring the qubits on and off resonance with a single (or a few) RF generator(s) with fixed frequency. This protocol is certainly feasible if all qubits have the same f_L and LSES, yet a large spread of these quantities may hinder its implementation. Note that due to restrictions in space and cooling power, including many RF generators on the chip is hardly possible.

In the present devices the electrical confinement is primarily controlled by the difference of potential V_C between the central and side gates. In order to assess the addressability of the qubits, we assume a single drive with frequency $f_0 = \overline{f_L}(V_C^0)$, and define a bias window $\delta V_C = V_C - V_C^0 \in [\delta V_C^{\min}, \delta V_C^{\max}]$ for device tuning (with V_C^0 the original bias such that $r_{\parallel}^0 = 28.3$ nm). We then count the fraction (yield) of qubits whose Larmor frequency f_L can be matched to f_0 within this window. For that purpose, we compute the g -matrix \hat{g} of each qubit at four different $\delta V_C = -40, -20, 0, 20$ mV and fit $f_L(\delta V_C)$ to a polynomial for each magnetic field orientation.

Note that constraints apply to δV_C , as the central gate potential must remain attractive enough to form the QD, yet shall not be too attractive to prevent the hole from escaping to the GeSi/Al₂O₃ interface. Additionally, large negative δV_C require a tight control over the barriers between the qubits to hold the quantum dot occupancy during manipulation. However, a given negative δV_C is roughly equivalent to a positive $\delta V = -\delta V_C$ on all side gates; it is, therefore, in principle possible to tune the confinement with minimal chemical potential variations across the dots using appropriate virtual gates (except in crossbar architectures). Taking these constraints into account, we consider asymmetric bias windows $\delta V_C \in [-2/3\Delta V_C, 1/3\Delta V_C]$. The map of the yield is plotted as a function of the orientation of the magnetic field in Fig. 11a for $n_i = 10^{11}$ cm⁻² and $\Delta V_C = 60$ mV. With lever-arms of the order of 0.2 eV/V, $\Delta V_C = 60$ mV is already > 4 times larger than U .

The yield is maximum (64%) at $\theta = 90^\circ$, where, surprisingly, the variability of g^* also peaks (see Sec. III B 1). Indeed, the yield decreases with $\mathcal{R}(f_L)$, but increases with the LSES of the C gate (better tunability). In the present devices, the decrease of the median LSES(C) (at constant Larmor frequency) is faster than the decrease of $\tilde{\mathcal{R}}(f_L)$ when the magnetic field goes slightly out-of-plane [50]. For $\theta = 90 \pm 2^\circ$, the fraction of tunable devices drops to 30%, which highlights the importance of a tight control over the orientation of \mathbf{B} . At large θ , $\tilde{\mathcal{R}}(f_L)$ however decreases faster than the LSES, and the yield increases again. As discussed previously, this region is hardly exploitable due to small Rabi frequencies. For in-plane magnetic fields, the yield is slightly smaller (54%) at $\varphi = \pm 45^\circ$ because the IQR of the g -factors are slightly larger than at $\varphi = 0^\circ$. The optimal magnetic field orientation for best qubit addressability is, therefore, $\mathbf{B} \parallel \mathbf{x}$.

We next set the magnetic field along this optimal orientation and plot the yield as a function of n_i and ΔV_C in Fig. 11b. Good addressability requires large bias

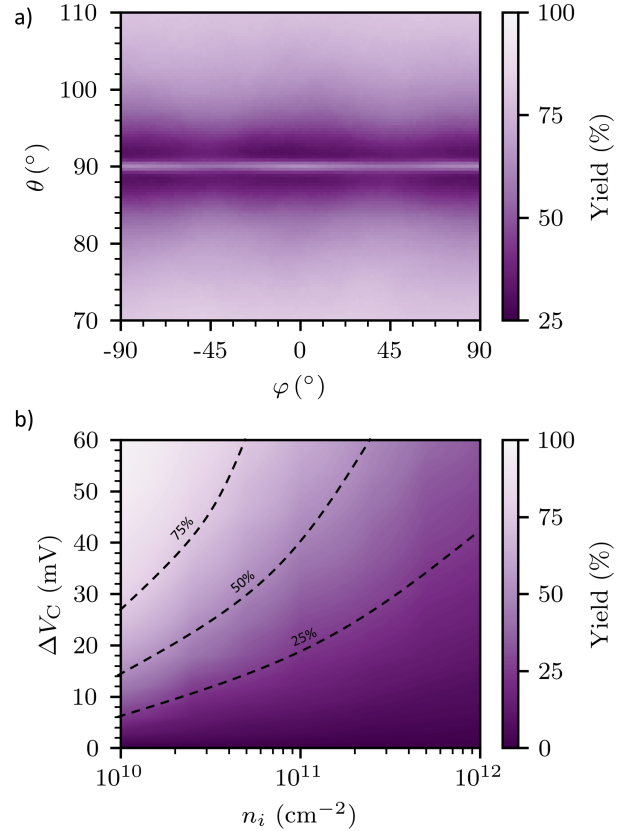


FIG. 11. a) Fraction of the devices whose Larmor frequency can be tuned to a target $f_L = \overline{f_L}$, as a function of the magnetic field orientation, allowing for a $\Delta V_C = 60$ mV bias corrections window. The trap density is $n_i = 10^{11}$ cm⁻². b) Fraction of the devices that can be tuned to the target $f_L = \overline{f_L}$ as a function of the bias window ΔV_C and n_i , for a magnetic field $\mathbf{B} \parallel \mathbf{x}$.

corrections even for moderate interface disorder. There are still $\sim 3\%$ of the devices that cannot be tuned at $n_i = 10^{10}$ cm⁻² and $\Delta V_C = 60$ mV. The situation worsens for larger n_i , as the yield is 64% for $n_i = 10^{11}$ cm⁻², and 33% for $n_i = 10^{12}$ cm⁻². As discussed above, $\Delta V_C = 60$ mV is already significantly larger than U , yet for smaller bias windows and standard interface qualities ($n_i = 10^{11} - 10^{12}$ cm⁻²), the yield barely reaches 50%.

In view of these results, it seems quite inevitable that each Ge qubit has to a large extent its own “spin personality”. In this respect, protocols trying to tune the qubits to a fixed RF signal may be challenging even at low n_i . Tuning the RF to each qubit may, on the other hand, compromise parallel operation. Spin manipulation by shuttling [44] appears, therefore, as a promising approach that turns the differences between the qubits into a resource, at the possible price of larger variability in the Rabi frequencies. In any case, it is clearly essential to take into account the variability of f_L when designing protocols for spin manipulation and shuttling in large-scale Ge architectures.

C. Processor quality factors

In this Subsection, we analyze the impact of the variability of Γ_2^* and f_R onto the performance of a large-scale quantum processor. The coherence of such a processor would be limited by the qubits with the largest dephasing rates Γ_2^* , whereas the operation times would be limited by the qubits with the slowest Rabi frequencies f_R (assuming that the two-qubit gates are fast enough not to limit the performances). Note that the slowest qubits and the ones with fastest decoherence are generally not the same. We can define the quality factor of a qubit as the number of π rotations that can be achieved within the dephasing time,

$$Q_2^* = 2f_R/\Gamma_2^*. \quad (12)$$

It is thus clear that the variability of f_R and Γ_2^* translates into a variability of Q_2^* . Along the lines of Ref. [37], we also define a quality factor for the whole quantum processor. For that purpose, we assume that we can discard the worst-performing qubits (the 5% slowest, and the 5% with fastest dephasing). With the remaining qubits, we compute

$$\hat{Q}_2^* = \min(f_R)/\max(\Gamma_2^*), \quad (13)$$

which is always smaller than \overline{Q}_2^* .

In Fig. 12a, we plot \hat{Q}_2^* as a function of the magnetic field orientation for the C, L and L+R drives and a charge trap density $n_i = 10^{11} \text{ cm}^{-2}$. In Fig. 12b, we also plot \hat{Q}_2^* , the median and IQR of Q_2^* , and the quality factor $\hat{Q}_2^{*,0}$ of the pristine device as a function of the angle θ for $\varphi = 0^\circ$. The C drive shows the smallest \overline{Q}_2^* owing to the slow f_R , and exhibits a significant IQR, fingerprint of the large variability in f_R (see Fig. 5). Moreover, the optimal operation point for this drive is in fact slightly out of plane ($\hat{Q}_2^* = 2$ for $\theta = 95^\circ$ and $\varphi = 45^\circ$, as \hat{Q}_2^* drastically drops down to ≈ 1 for $\theta \rightarrow 90^\circ$). This is the consequence of having at least one qubit with low enough disorder so that $f_R \approx 0$ for in-plane magnetic fields. In the absence of disorder, the in-plane quality factor is indeed zero as $f_R \rightarrow 0$.

The L and L+R drives perform similarly. The anisotropy of Q_2^* is dominated by the variations of f_R , which peaks in-plane. \overline{Q}_2^* shows the same qualitative behavior as the pristine device, and reaches 17 for the L and 16 for the L+R drive at $\theta = 90^\circ$, $\varphi = 0^\circ$. The IQR also highlights a significant spread of the quality factors, with $\mathcal{R}(Q_2^*) \approx 5.5$ for both drives at the same magnetic field orientation. The maximal \hat{Q}_2^* is achieved at $\theta = 90^\circ$ and is 7.7 for L and 7.2 for L+R drives. The optimal magnetic field orientation for these drives is therefore in-plane, which ensures both best qubits on average and the best performance for the quantum processor as a whole.

V. CONCLUSIONS

In this study, we have quantified the variability of the charge and spin properties of Ge spin qubits resulting from interface traps at the top SiGe/oxide interface. Our analysis reveals a moderate variability of charge properties, with ensemble values notably better than those reported for Si MOS devices. However, the variability of spin properties remains significant. This is primarily attributed to the diverse spin-orbit coupling mechanisms at work in Ge and, in particular, to the pronounced sensitivity of in-plane g -factors to modulations of the QD size and shape, and of f_R to local strains. We find that driving the qubits with one (or two) side gates is more robust against disorder than driving with the plunger gate; yet achieving variabilities below 10% in both the Larmor and Rabi frequencies calls for trap densities $n_i \lesssim 10^{10} \text{ cm}^{-2}$.

We have also assessed the implications of variability. We have explored the effect of chemical potential fluctuations on the operation of crossbar architectures. Despite the relatively low variability of this chemical potential, our findings indicate that crossbar architectures may require state-of-the-art interface quality to ensure single-hole occupancy in all qubits. The variability of in-plane g -factors also poses a significant challenge for manipulation protocols relying on Stark shifts to bring qubits in and out of resonance with a RF signal. This highlights the need to account for this variability in the design of protocols for large-scale spin manipulation. Similarly, the distribution of Rabi frequencies and decoherence times can impact the performance of quantum processors. We find that the optimal magnetic field orientation for Ge qubits, that minimizes the impact of disorder and maximizes the quality of the qubits and quantum processor is in plane when driving with side gate(s), and a few degrees out-of-plane when driving with the plunger gate.

Overall, this study underscores the critical importance of material and interface quality in achieving homogeneous and reproducible qubits. Despite the lower intrinsic disorder in Ge/GeSi heterostructures, variability remains a significant challenge when scaling up quantum devices. The vision of large-scale quantum architectures with homogeneous qubits appears, therefore, little realistic. Instead, each qubit shows its own personality to some extent, and quantum manipulation protocols and hardware must be able to cope with this variety, and even turn it into a resource [44].

ACKNOWLEDGEMENTS

We thank Cécile Yu, Esteban A. Rodriguez-Mena, and José-Carlos Garcia Abadillo-Uriel for fruitful discussions. This work was supported by the ‘‘France 2030’’ program (PEPR PRESQUILE-ANR-22-PETQ-0002) and by the Horizon Europe Framework Program (grant agreement 101174557 QLSI2).

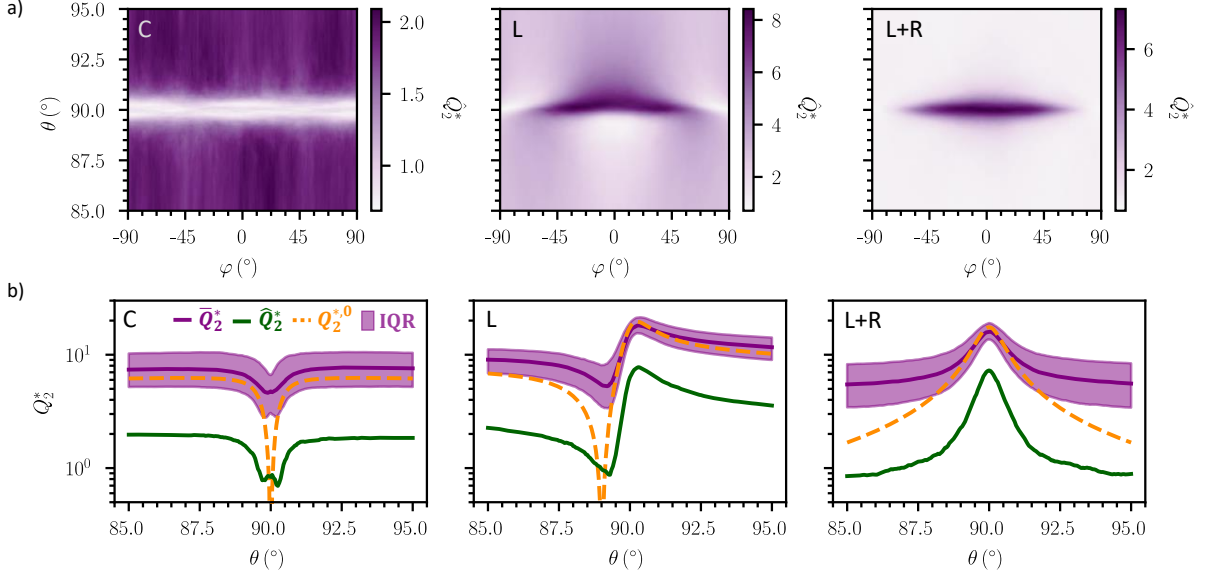


FIG. 12. Quality factors in disordered devices. a) Quality factor \hat{Q}_2^* of the quantum processor as a function of the magnetic field orientation for $n_i = 10^{11} \text{ cm}^{-2}$ and a drive with the C, L and L+R gates. b) Median \bar{Q}_2^* and IQR $\mathcal{R}(Q_2^*)$ of the quality factor of the qubits, quality factor \hat{Q}_2^* of the processor, and quality factor $Q_2^{*,0}$ of the pristine device as a function of the angle θ of the magnetic field ($\varphi = 0^\circ$), for $n_i = 10^{11} \text{ cm}^{-2}$ and the same three drives as in a).

Appendix A: Surface roughness variability

In this work, we have focused on charge traps at the SiGe/oxide interface as the source of disorder. Indeed, epitaxial interfaces are expected to be free of such traps, but they may be interdiffused and rough. The correlation length ($L_C \sim 50 - 100 \text{ nm}$) and rms amplitude ($\delta z_{\text{rms}} \sim 0.2 - 0.7 \text{ nm}$) of this roughness have been characterized for Si/SiGe heterostructures [56]. L_C is thus comparable or larger than the typical dot size ($2r_{\parallel} \approx 56 \text{ nm}$ in this study), so that the interface can be considered, in a first approximation, almost flat at the scale of each QD. Nonetheless, such roughness gives rise to qubit-to-qubit fluctuations of the quantum well thickness at larger scale, and may thus contribute to the variability in arrays. Although L_C and δz_{rms} have not been measured for Ge/SiGe, we expect the order of magnitude to be similar.

In order to quantify the impact of thickness fluctuations on variability, we consider a pristine Ge qubit ($n_i = 0$), and compute the dependence of the g -factors and Rabi frequencies on the well thickness H_{Ge} . The data for g_x^0 , g_y^0 , g_z^0 and for the Rabi frequency $f_{R,x}^0$ ($\mathbf{B} \parallel \mathbf{x}$, L and L+R drives) are plotted in Fig. 13. Note that we did not include the C drive as $f_{R,x}^0 = 0$ for the pristine device. Also, the charge properties remain almost constant since the radius of the QD is kept fixed ($r_{\parallel}^0 = 28.3 \text{ nm}$).

We find that fluctuations of the Ge well thickness by $3\delta z_{\text{rms}} \approx 2 \text{ nm}$ induce variations of the in-plane g -factors by roughly 3%. The out-of-plane g -factor, which showed remarkably low variability for charge defects, can vary by up to 5% (due to the strong dependence of g_z on vertical

confinement [37, 79]). The impact on $f_{R,x}^0$ is even larger, with variations that can reach 10%. Still, these figures are all smaller than the $\tilde{\mathcal{R}}$'s reported in the main text, so that charge traps usually dominate the overall variability. Long-range fluctuations of H_{Ge} may however become significant in devices where the influence of charge traps has been reduced. This could be achieved, for example, by increasing H_{SiGe} as shown in Appendix D, or by engineering the gate layout as discussed in Ref. [55].

Appendix B: Variability in absence of cooling strains and in presence of uniaxial strains

Ge hole spins are extremely sensitive to strains. The inhomogeneous strains imprinted by the differential thermal contraction of materials are, notably, a key ingredient for spin manipulation with in-plane magnetic fields [54]. Although strains are not disordered in the present study, they may contribute to the variability of the spin properties as the dot moves in the inhomogeneously deformed crystal under the action of the traps. It is not, therefore, trivial to conclude whether inhomogeneous strains are an asset or a liability. In this Appendix, we discuss variability in the absence of cool-down strains.

The relative IQRs of the effective g -factors g_x , g_y and g_z are plotted as a function of n_i in Fig. 14. They are similar to those in inhomogeneous strains (see Fig. 4a). This shows that the variability of the g -factors is mainly due to the disorder-induced deformations of the QDs rather than to their displacements in the inhomogeneous strains. The absolute IQR of $f_{R,x}$ decreases but

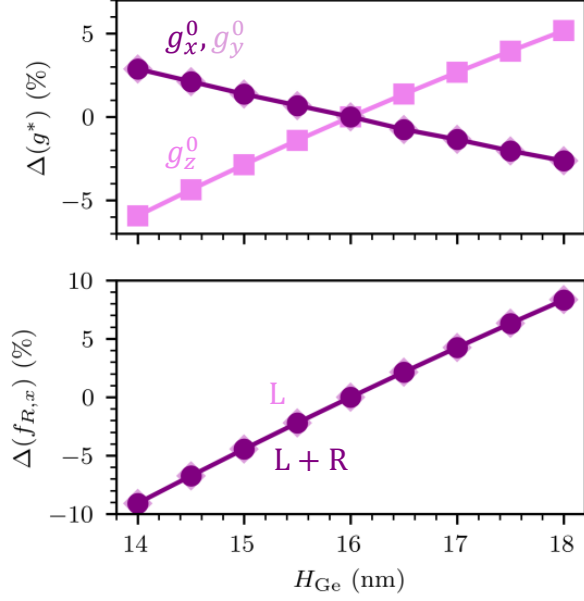


FIG. 13. a) Dependence of the g -factors g_x^0 , g_y^0 , g_z^0 of the pristine device ($n_i = 0$) on the thickness H_{Ge} of the Ge film. The variations $\Delta(g^*) = (g^* - g_{\text{ref}}^*)/g_{\text{ref}}^*$ are computed with respect to the reference g_{ref}^* at $H_{\text{Ge}} = 16$ nm. b) Dependence of $f_{R,x}^0$ on H_{Ge} (L and L+R drives). Note that $f_{R,x}^0 = 0$ for the C drive. V_C is adjusted so that $r_{\parallel}^0 = 28.3$ nm for all H_{Ge} .

the relative IQR $\tilde{\mathcal{R}}(f_{R,x})$ remains, nevertheless, close to 100% for all drives and n_i (data not shown) because the median Rabi frequencies at $f_L^0 = 2$ GHz drop close to 1 MHz. This is in line with the results of Fig. 6, and the conclusion that inhomogeneous strains are the main mechanism for Rabi oscillations.

A recent work has highlighted the strong impact of uniaxial strains on the gyromagnetic factors of heavy-holes [67]. The small in-plane g -factors can, indeed, be greatly enhanced by the introduction of uniaxial strains $\varepsilon_{xx} \neq \varepsilon_{yy}$. As an illustration, we plot in Fig. 6 the relative IQR of g_x , g_y and g_z as a function of n_i for homogeneous uniaxial strains $(\varepsilon_{xx} - \varepsilon_{yy})/(2\varepsilon_{\parallel}) = -10\%$. The g -factors of the pristine device (with a uniform charge distribution $n_i = 10^{11}$ cm $^{-2}$) are now $g_x^0 = 0.62$ and $g_y^0 = 0.39$. This large increase of the in-plane g -factors actually results in a reduction of $\tilde{\mathcal{R}}(g_x^*)$ and $\tilde{\mathcal{R}}(g_y^*)$ by almost a factor 4. Moreover, uniaxial strains efficiently lock the in-plane magnetic axes along x and y (more generally, along the directions parallel and perpendicular to the uniaxial axis). The φ_g 's are now distributed around 0 with a full width at half-maximum of only $\approx 2^\circ$. This has important consequences for spin manipulation by shuttling [44]: in the absence of large rotations φ_g , the required imbalance between the precession axes of the dots is only controlled by the principal g -factors g_x and g_y ; this reduces the probability that neighboring dots have very different random precession axes, but opens the way

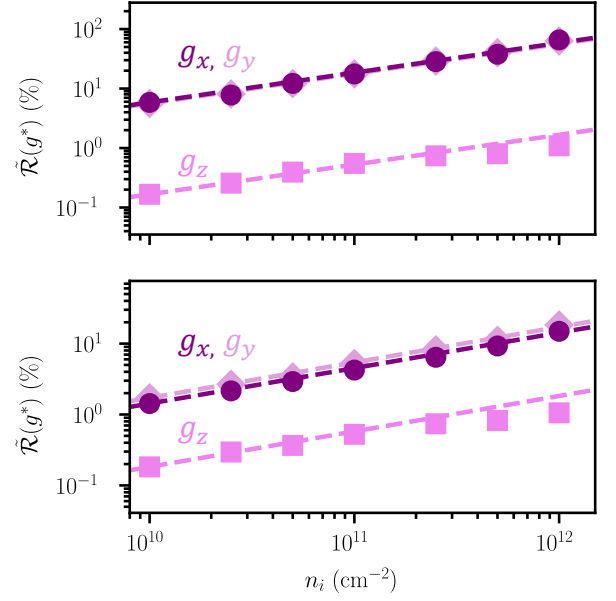


FIG. 14. a) Relative IQR $\tilde{\mathcal{R}}$ of the g -factors g_x , g_y and g_z as a function of n_i , in the absence of inhomogeneous cool-down strains. b) Same with uniform uniaxial strains $(\varepsilon_{xx} - \varepsilon_{yy})/(2\varepsilon_{\parallel}) = -10\%$. The calculations are performed at the same V_C as in Fig. 2.

for a careful control of these axes by the gate voltages. These results show that strain engineering can be an effective strategy to mitigate variability in Ge.

Appendix C: Effect of confinement on variability

All calculations in the main text are performed at the bias V_C such that the radius of the pristine QD is $r_{\parallel} = r_{\parallel}^0 = 28.3$ nm. This choice is realistic but, nevertheless, arbitrary. In this Appendix, we discuss the dependence of the variability of the charge and spin properties on the confinement strength (i.e., on V_C) for a trap density $n_i = 10^{11}$ cm $^{-2}$. It is worth reminding that this strength is limited by the band offset between Ge and SiGe, and by the thickness of the top SiGe barrier, as the hole ultimately escapes the quantum well and gets confined at the SiGe/oxide interface at large vertical electric fields.

Fig. 15a shows the dependence of $\mathcal{R}(\Delta\mu)$ and $\mathcal{R}(r_{\parallel})$ on V_C . While the spread of the QD size is reduced by stronger confinement (more negative V_C), the IQR of $\Delta\mu$ shows on the opposite a slight increase. Similarly, we plot in Fig. 15b the relative IQR of g_x , g_y , and g_z as a function of V_C , as well as the relative IQR $\tilde{\mathcal{R}}(f_{R,x})$ of the Rabi frequency for the C, L and L+R drives with $\mathbf{B} \parallel \mathbf{x}$. They only decrease slightly when V_C is pulled down. Note that stronger confinement reduces \mathcal{R} , but comes along with a decrease of the median g_x , g_y and $f_{R,x}$

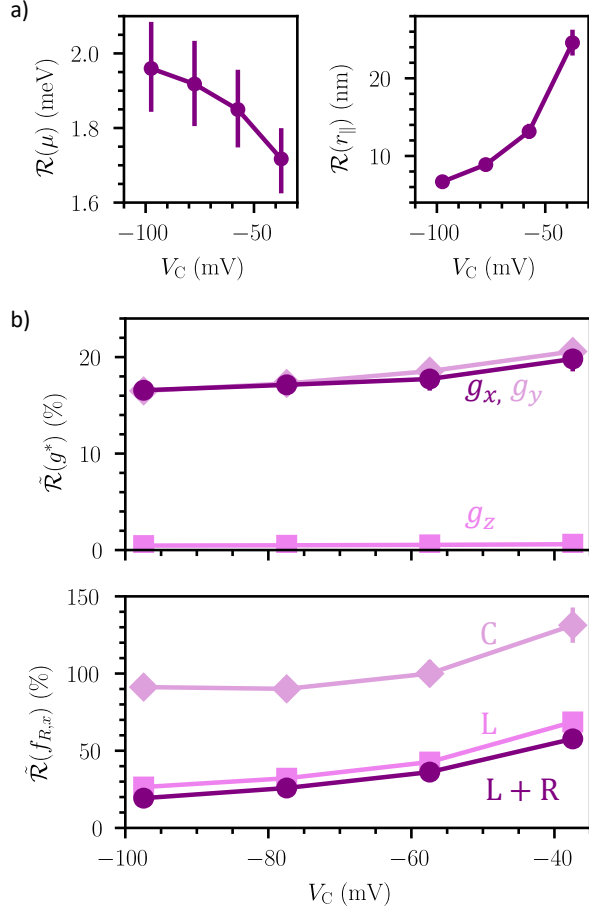


FIG. 15. Dependence of the variability on V_C . a) $\mathcal{R}(\mu)$ and $\mathcal{R}(r_{\parallel})$ as a function of V_C for $n_i = 10^{11} \text{ cm}^{-2}$. The error bars are the 95% confidence intervals. b) Relative IQR $\tilde{\mathcal{R}}$ of the g -factors g_x , g_y and g_z , and of f_R (for $\mathbf{B} \parallel \mathbf{x}$ and the C, L and L+R drives) as a function of V_C . The data for g_x and g_y are slightly different because the statistics were computed on a smaller set of 500 devices.

that smoothes the variations of $\tilde{\mathcal{R}}$. Working with strongly confined QDs can, therefore, homogenize the position and size of the QDs, but does not substantially improve the relative variability of the spin properties.

Appendix D: Dependence of variability on the top SiGe barrier thickness

The thickness H_{SiGe} of the top SiGe barrier has a large impact on variability. A thicker barrier indeed shifts the defective interface with the oxide further away from the QDs, at the expense of a weaker electrostatic control (the gates being also farther). As an illustration, we compute the variability due to interface traps with density $n_i = 10^{11} \text{ cm}^{-2}$ in devices with $H_{\text{SiGe}} = 10, 30$ and 70 nm . As in the main text, we set V_C so that the radius of the pristine QDs is $r_{\parallel} = 28.3 \text{ nm}$. The results are shown in

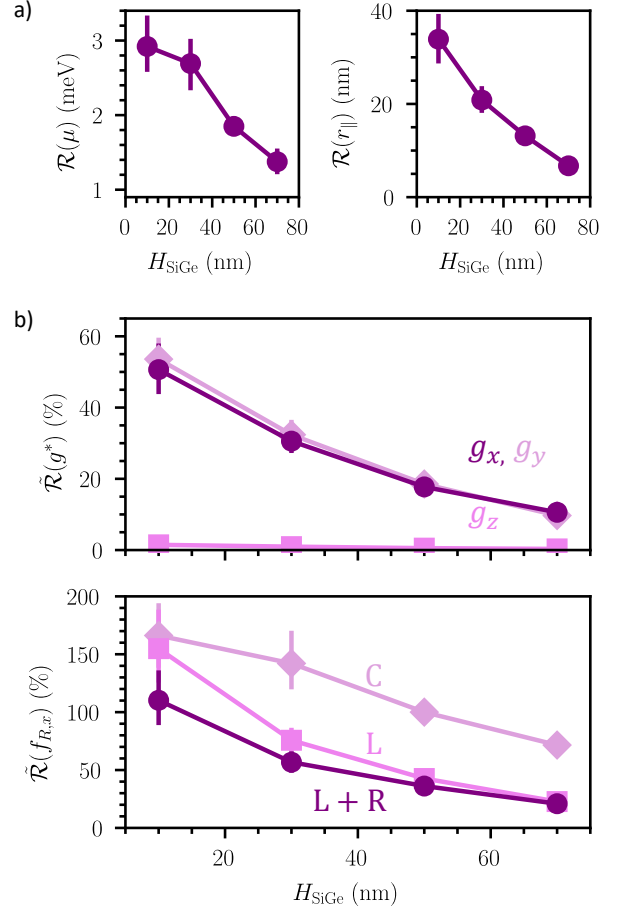


FIG. 16. Dependence of the variability on the top SiGe barrier thickness. a) $\mathcal{R}(\mu)$ and $\mathcal{R}(r_{\parallel})$ as a function of H_{SiGe} for $n_i = 10^{11} \text{ cm}^{-2}$ and V_C adjusted so that $r_{\parallel} = 28.3 \text{ nm}$ in the pristine QDs. The error bars are the 95% confidence intervals. b) Relative IQR $\tilde{\mathcal{R}}$ of the g -factors g_x , g_y and g_z , and of f_R (for $\mathbf{B} \parallel \mathbf{x}$ and the C, L and L+R drives) as a function of H_{SiGe} . The data for g_x and g_y are slightly different because the statistics were computed on a smaller set of 500 devices.

Fig. 16.

With respect to $H_{\text{SiGe}} = 50 \text{ nm}$ (main text), reducing the barrier thickness substantially increases the spread of both charge and spin properties. At $H_{\text{SiGe}} = 10 \text{ nm}$, the absolute IQRs of μ and d_{\parallel} are $\mathcal{R}(\mu) = 2.9 \text{ meV}$ and $\mathcal{R}(d_{\parallel}) = 34 \text{ nm}$, and the relative IQRs or the Larmor and Rabi frequencies are $\tilde{\mathcal{R}}(f_L) \approx 50\%$ and $\tilde{\mathcal{R}}(f_R) \approx 100\%$ (for in-plane magnetic fields). On the opposite, increasing H_{SiGe} beyond 50 nm further helps to mitigate the variability, with $\mathcal{R}(\mu) < 1.5 \text{ meV}$, $\mathcal{R}(d_{\parallel}) < 10 \text{ nm}$, and $\tilde{\mathcal{R}}(f_L, f_R) < 20\%$ achievable for $H_{\text{SiGe}} \gtrsim 70 \text{ nm}$. Moreover, the loss of electrostatic control is in fact moderate, as the lever-arm of the C gate only decreases from 0.2 to 0.16 , which results in $V_C(r_{\parallel} = 28.3 \text{ nm}) = 87 \text{ mV}$ (as compared to $V_C(r_{\parallel} = 28.3 \text{ nm}) = 58 \text{ mV}$ for $H_{\text{SiGe}} = 50 \text{ nm}$). Consequently, increasing H_{SiGe} can be an effective measure to reduce variability. This conclusion is in line with

recent mobility measurements in devices with thick SiGe barriers [80]. Alternative gate layouts have also been

proposed to mitigate variability while preserving a good electrostatic control [55].

-
- [1] D. Loss and D. P. DiVincenzo, Quantum computation with quantum dots, *Physical Review A* **57**, 120 (1998).
- [2] R. Hanson, L. P. Kouwenhoven, J. R. Petta, S. Tarucha, and L. M. K. Vandersypen, Spins in few-electron quantum dots, *Rev. Mod. Phys.* **79**, 1217 (2007).
- [3] J. R. Petta, A. C. Johnson, J. M. Taylor, E. A. Laird, A. Yacoby, M. D. Lukin, C. M. Marcus, M. P. Hanson, and A. C. Gossard, Coherent manipulation of coupled electron spins in semiconductor quantum dots, *Science* **309**, 2180 (2005).
- [4] P.-A. Mortemousque, E. Chanrion, B. Jadot, H. Flentje, A. Ludwig, A. D. Wieck, M. Urdampilleta, C. Bäuerle, and T. Meunier, Coherent control of individual electron spins in a two-dimensional quantum dot array, *Nature Nanotechnology* **16**, 296 (2021).
- [5] R. Maurand, X. Jehl, D. Kotekar-Patil, A. Corna, H. Bohoslavskyi, R. Laviéville, L. Hutin, S. Barraud, M. Vinet, M. Sanquer, and S. De Franceschi, A CMOS silicon spin qubit, *Nature Communications* **7**, 13575 (2016).
- [6] S. Geyer, B. Hetényi, S. Bosco, L. C. Camenzind, R. S. Egli, A. Fuhrer, D. Loss, R. J. Warburton, D. M. Zumbühl, and A. V. Kuhlmann, Anisotropic exchange interaction of two hole-spin qubits, *Nature Physics* **20**, 1152 (2024).
- [7] B. Klemt, V. Elhomsy, M. Nurizzo, P. Hamonic, B. Martinez, B. Cardoso Paz, C. Spence, M. C. Dartiaillh, B. Jadot, E. Chanrion, V. Thiney, R. Lethiecq, B. Bertrand, H. Niebojewski, C. Bäuerle, M. Vinet, Y.-M. Niquet, T. Meunier, and M. Urdampilleta, Electrical manipulation of a single electron spin in cmos using a micromagnet and spin-valley coupling, *npj Quantum Information* **9**, 107 (2023).
- [8] C. H. Yang, R. C. C. Leon, J. C. C. Hwang, A. Saraiva, T. Tantt, W. Huang, J. Camirand Lemyre, K. W. Chan, K. Y. Tan, F. E. Hudson, K. M. Itoh, A. Morello, M. Pioro-Ladrière, A. Laucht, and A. S. Dzurak, Operation of a silicon quantum processor unit cell above one kelvin, *Nature* **580**, 350 (2020).
- [9] S. G. J. Philips, M. T. Mądzik, S. V. Amitonov, S. L. de Snoo, M. Russ, N. Kalhor, C. Volk, W. I. L. Lawrie, D. Brousse, L. Tryputen, B. P. Wuetz, A. Sammak, M. Veldhorst, G. Scappucci, and L. M. K. Vandersypen, Universal control of a six-qubit quantum processor in silicon, *Nature* **609**, 919 (2022).
- [10] J. Yoneda, K. Takeda, T. Otsuka, T. Nakajima, M. R. Delbecq, G. Allison, T. Honda, T. Kodera, S. Oda, Y. Hoshi, N. Usami, K. M. Itoh, and S. Tarucha, A quantum-dot spin qubit with coherence limited by charge noise and fidelity higher than 99.9%, *Nature Nanotechnology* **13**, 102 (2018).
- [11] T. Koch, C. Godfrin, V. Adam, J. Ferrero, D. Schroller, N. Glaeser, S. Kubicek, R. Li, R. Loo, S. Massar, G. Simion, D. Wan, K. De Greve, and W. Wernsdorfer, Industrial 300 mm wafer processed spin qubits in natural silicon/silicon-germanium, *npj Quantum Information* **11**, 59 (2025).
- [12] N. W. Hendrickx, D. P. Franke, A. Sammak, G. Scappucci, and M. Veldhorst, Fast two-qubit logic with holes in germanium, *Nature* **577**, 487 (2020).
- [13] D. Jirovec, A. Hofmann, A. Ballabio, P. M. Mutter, G. Tavani, M. Botifoll, A. Crippa, J. Kukucka, O. Sagi, F. Martins, J. Saez-Mollejo, I. Prieto, M. Borovkov, J. Arbiol, D. Chrastina, G. Isella, and G. Katsaros, A singlet-triplet hole spin qubit in planar ge, *Nature Materials* **20**, 1106 (2021).
- [14] N. W. Hendrickx, W. I. L. Lawrie, M. Russ, F. van Riggele, S. L. de Snoo, R. N. Schouten, A. Sammak, G. Scappucci, and M. Veldhorst, A four-qubit germanium quantum processor, *Nature* **591**, 580 (2021).
- [15] N. W. Hendrickx, L. Massai, M. Mergenthaler, F. J. Schupp, S. Paredes, S. W. Bedell, G. Salis, and A. Fuhrer, Sweet-spot operation of a germanium hole spin qubit with highly anisotropic noise sensitivity, *Nature Materials* **23**, 920 (2024).
- [16] V. John, C. X. Yu, B. van Straaten, E. A. Rodríguez-Mena, M. Rodríguez, S. Oosterhout, L. E. A. Stehouwer, G. Scappucci, S. Bosco, M. Rimbach-Russ, Y.-M. Niquet, F. Borsoi, and M. Veldhorst, *A two-dimensional 10-qubit array in germanium with robust and localised qubit control* (2024), [arXiv:2412.16044 \[cond-mat.mes-hall\]](https://arxiv.org/abs/2412.16044).
- [17] T. Struck, A. Hollmann, F. Schauer, O. Fedorets, A. Schmidbauer, K. Sawano, H. Riemann, N. V. Abrosimov, Ł. Cywiński, D. Bougeard, and L. R. Schreiber, Low-frequency spin qubit energy splitting noise in highly purified $^{28}\text{Si}/\text{SiGe}$, *npj Quantum Information* **6**, 40 (2020).
- [18] F. K. Unseld, M. Meyer, M. T. Mądzik, F. Borsoi, S. L. de Snoo, S. V. Amitonov, A. Sammak, G. Scappucci, M. Veldhorst, and L. M. K. Vandersypen, A 2D quantum dot array in planar $^{28}\text{Si}/\text{SiGe}$, *Applied Physics Letters* **123**, 084002 (2023).
- [19] P. Stano and D. Loss, Review of performance metrics of spin qubits in gated semiconducting nanostructures, *Nature Reviews Physics* **4**, 672 (2022).
- [20] L. Cvitkovich, P. Stano, C. Wilhelmer, D. Waldhör, D. Loss, Y.-M. Niquet, and T. Grasser, *Coherence limit due to hyperfine interaction with nuclei in the barrier material of si spin qubits* (2024), [arXiv:2405.10667 \[cond-mat.mes-hall\]](https://arxiv.org/abs/2405.10667).
- [21] X. Xue, M. Russ, N. Samkharadze, B. Undseth, A. Sammak, G. Scappucci, and L. M. K. Vandersypen, Quantum logic with spin qubits crossing the surface code threshold, *Nature* **601**, 343 (2022).
- [22] P. Steinacker, N. D. Stuyck, W. H. Lim, T. Tantt, M. Feng, A. Nickl, S. Serrano, M. Candido, J. D. Cifuentes, F. E. Hudson, K. W. Chan, S. Kubicek, J. Jusot, Y. Canvel, S. Beyne, Y. Shimura, R. Loo, C. Godfrin, B. Raes, S. Baudot, D. Wan, A. Laucht, C. H. Yang, A. Saraiva, C. C. Escott, K. D. Greve, and A. S. Dzurak, *A 300 mm foundry silicon spin qubit unit cell exceeding 99% fidelity in all operations* (2024), [arXiv:2410.15590 \[cond-mat.mes-hall\]](https://arxiv.org/abs/2410.15590).
- [23] J. Y. Huang, R. Y. Su, W. H. Lim, M. Feng, B. van Straaten, B. Severin, W. Gilbert, N. Dumoulin Stuyck,

- T. Tantt, S. Serrano, J. D. Cifuentes, I. Hansen, A. E. Seedhouse, E. Vahapoglu, R. C. C. Leon, N. V. Abrosimov, H.-J. Pohl, M. L. W. Thewalt, F. E. Hudson, C. C. Escott, N. Ares, S. D. Bartlett, A. Morello, A. Saraiva, A. Laucht, A. S. Dzurak, and C. H. Yang, High-fidelity spin qubit operation and algorithmic initialization above 1 K, *Nature* **627**, 772 (2024).
- [24] A. Noiri, K. Takeda, T. Nakajima, T. Kobayashi, A. Sammak, G. Scappucci, and S. Tarucha, A shuttling-based two-qubit logic gate for linking distant silicon quantum processors, *Nature Communications* **13**, 5740 (2022).
- [25] I. Seidler, T. Struck, R. Xue, N. Focke, S. Trellenkamp, H. Bluhm, and L. R. Schreiber, Conveyor-mode single-electron shuttling in si/sige for a scalable quantum computing architecture, *npj Quantum Information* **8**, 100 (2022).
- [26] F. van Riggelen-Doelman, C.-A. Wang, S. L. de Snoo, W. I. L. Lawrie, N. W. Hendrickx, M. Rimbach-Russ, A. Sammak, G. Scappucci, C. Déprez, and M. Veldhorst, Coherent spin qubit shuttling through germanium quantum dots, *Nature Communications* **15**, 5716 (2024).
- [27] N. Samkharadze, G. Zheng, N. Kalhor, D. Brousse, A. Sammak, U. C. Mendes, A. Blais, G. Scappucci, and L. M. K. Vandersypen, Strong spin-photon coupling in silicon, *Science* **359**, 1123 (2018).
- [28] C. X. Yu, S. Zihlmann, J. C. Abadillo-Uriel, V. P. Michal, N. Rambal, H. Niebojewski, T. Bedecarrats, M. Vinet, É. Dumur, M. Filippone, B. Bertrand, S. De Franceschi, Y.-M. Niquet, and R. Maurand, Strong coupling between a photon and a hole spin in silicon, *Nature Nanotechnology* **18**, 741 (2023).
- [29] J. Dijkema, X. Xue, P. Harvey-Collard, M. Rimbach-Russ, S. L. de Snoo, G. Zheng, A. Sammak, G. Scappucci, and L. M. K. Vandersypen, Cavity-mediated iswap oscillations between distant spins, *Nature Physics* **21**, 168 (2025).
- [30] F. Borsoi, N. W. Hendrickx, V. John, M. Meyer, S. Motz, F. van Riggelen, A. Sammak, S. L. de Snoo, G. Scappucci, and M. Veldhorst, Shared control of a 16 semiconductor quantum dot crossbar array, *Nature Nanotechnology* **19**, 21 (2024).
- [31] W. Han Lim, T. Tantt, T. Youn, J. Y. Huang, S. Serrano, A. Dickie, S. Yianni, F. E. Hudson, C. C. Escott, C. H. Yang, A. Laucht, A. Saraiva, K. W. Chan, J. D. Cifuentes, and A. S. Dzurak, A 2×2 quantum dot array in silicon with fully tunable pairwise interdot coupling, *Nano Letters* (2025).
- [32] L. M. K. Vandersypen, H. Bluhm, J. S. Clarke, A. S. Dzurak, R. Ishihara, A. Morello, D. J. Reilly, L. R. Schreiber, and M. Veldhorst, Interfacing spin qubits in quantum dots and donors – hot, dense, and coherent, *npj Quantum Information* **3**, 34 (2017).
- [33] M. Vinet, L. Hutin, B. Bertrand, S. Barraud, J.-M. Hartmann, Y.-J. Kim, V. Mazzocchi, A. Amisse, H. Bohuslavskyi, L. Bourdet, A. Crippa, X. Jehl, R. Maurand, Y.-M. Niquet, M. Sanquer, B. Venitucci, B. Jadot, E. Chanrion, P.-A. Mortemousque, C. Spence, M. Urdampilleta, S. De Franceschi, and T. Meunier, in *2018 IEEE International Electron Devices Meeting (IEDM)* (2018) p. 6.5.1, Towards scalable silicon quantum computing.
- [34] M. Künne, A. Willmes, M. Oberländer, C. Gorjaew, J. D. Teske, H. Bhardwaj, M. Beer, E. Kammerloher, R. Otten, I. Seidler, R. Xue, L. R. Schreiber, and H. Bluhm, The spinbus architecture for scaling spin qubits with electron shuttling, *Nature Communications* **15**, 4977 (2024).
- [35] S. De Franceschi, L. Hutin, R. Maurand, L. Bourdet, H. Bohuslavskyi, A. Corna, D. Kotekar-Patil, S. Barraud, X. Jehl, Y.-M. Niquet, M. Sanquer, and M. Vinet, in *2016 IEEE International Electron Devices Meeting (IEDM)* (2016) p. 13.4.1, SOI technology for quantum information processing.
- [36] M. Vinet, The path to scalable quantum computing with Silicon spin qubits, *Nature Nanotechnology* **16**, 1296 (2021).
- [37] B. Martinez and Y.-M. Niquet, Variability of electron and hole spin qubits due to interface roughness and charge traps, *Physical Review Applied* **17**, 024022 (2022).
- [38] J. D. Cifuentes, T. Tantt, W. Gilbert, J. Y. Huang, E. Vahapoglu, R. C. C. Leon, S. Serrano, D. Otter, D. Dunmore, P. Y. Mai, F. Schlattner, M. Feng, K. Itoh, N. Abrosimov, H.-J. Pohl, M. Thewalt, A. Laucht, C. H. Yang, C. C. Escott, W. H. Lim, F. E. Hudson, R. Rahman, A. S. Dzurak, and A. Saraiva, Bounds to electron spin qubit variability for scalable cmos architectures, *Nature Communications* **15**, 4299 (2024).
- [39] A. Sammak, D. Sabbagh, N. W. Hendrickx, M. Lodari, B. Paquelet Wuetz, A. Tosato, L. Yeoh, M. Bollani, M. Virgilio, M. A. Schubert, P. Zaumseil, G. Capellini, M. Veldhorst, and G. Scappucci, Shallow and undoped germanium quantum wells: A playground for spin and hybrid quantum technology, *Advanced Functional Materials* **29**, 1807613 (2019).
- [40] G. Scappucci, C. Kloeffel, F. A. Zwanenburg, D. Loss, M. Myronov, J.-J. Zhang, S. De Franceschi, G. Katsaros, and M. Veldhorst, The germanium quantum information route, *Nature Reviews Materials* **6**, 926 (2021).
- [41] G. Scappucci, P. J. Taylor, J. R. Williams, T. Ginley, and S. Law, Crystalline materials for quantum computing: Semiconductor heterostructures and topological insulators exemplars, *MRS Bulletin* **46**, 596 (2021).
- [42] D. Degli Esposti, L. E. A. Stehouwer, Ö. Gül, N. Samkharadze, C. Déprez, M. Meyer, I. N. Meijer, L. Tryputen, S. Karwal, M. Botifoll, J. Arbiol, S. V. Amitonov, L. M. K. Vandersypen, A. Sammak, M. Veldhorst, and G. Scappucci, Low disorder and high valley splitting in silicon, *npj Quantum Information* **10**, 32 (2024).
- [43] K. Takeda, A. Noiri, T. Nakajima, J. Yoneda, T. Kobayashi, and S. Tarucha, Quantum tomography of an entangled three-qubit state in silicon, *Nature Nanotechnology* **16**, 965 (2021).
- [44] C.-A. Wang, V. John, H. Tidjani, C. X. Yu, A. S. Ivlev, C. Déprez, F. van Riggelen-Doelman, B. D. Woods, N. W. Hendrickx, W. I. L. Lawrie, L. E. A. Stehouwer, S. D. Oosterhout, A. Sammak, M. Friesen, G. Scappucci, S. L. de Snoo, M. Rimbach-Russ, F. Borsoi, and M. Veldhorst, Operating semiconductor quantum processors with hopping spins, *Science* **385**, 447 (2024).
- [45] A. Tosato, A. Elsayed, F. Poggiali, L. Stehouwer, D. Costa, K. Hudson, D. D. Esposti, and G. Scappucci, *Qarpet: A crossbar chip for benchmarking semiconductor spin qubits* (2025), arXiv:2504.05460 [cond-mat.mes-hall].
- [46] C.-A. Wang, C. Déprez, H. Tidjani, W. I. L. Lawrie, N. W. Hendrickx, A. Sammak, G. Scappucci, and M. Veldhorst, Probing resonating valence bonds on a programmable germanium quantum simulator, *npj Quantum*

- tum Information **9**, 58 (2023).
- [47] X. Zhang, E. Morozova, M. Rimbach-Russ, D. Jirovec, T.-K. Hsiao, P. C. Fariña, C.-A. Wang, S. D. Oosterhout, A. Sammak, G. Scappucci, M. Veldhorst, and L. M. K. Vandersypen, Universal control of four singlet-triplet qubits, *Nature Nanotechnology* **20**, 209 (2025).
- [48] V. N. Golovach, M. Borhani, and D. Loss, Electric-dipole-induced spin resonance in quantum dots, *Phys. Rev. B* **74**, 165319 (2006).
- [49] N. Piot, B. Brun, V. Schmitt, S. Zihlmann, V. P. Michal, A. Apra, J. C. Abadillo-Uriel, X. Jehl, B. Bertrand, H. Niebojewski, L. Hutin, M. Vinet, M. Urdampilleta, T. Meunier, Y.-M. Niquet, R. Maurand, and S. D. Franceschi, A single hole spin with enhanced coherence in natural silicon, *Nature Nanotechnology* **17**, 1072 (2022).
- [50] L. Mauro, E. A. Rodríguez-Mena, M. Bassi, V. Schmitt, and Y.-M. Niquet, Geometry of the dephasing sweet spots of spin-orbit qubits, *Phys. Rev. B* **109**, 155406 (2024).
- [51] M. J. Carballido, S. Svab, R. S. Eggli, T. Patlatiuk, P. C. Kwon, J. Schuff, R. M. Kaiser, L. C. Camenzind, A. Li, N. Ares, E. P. A. M. Bakkers, S. Bosco, J. C. Egues, D. Loss, and D. M. Zumbühl, *Compromise-Free Scaling of Qubit Speed and Coherence* (2024), arXiv:2402.07313 [cond-mat.mes-hall].
- [52] M. Bassi, E.-A. Rodríguez-Mena, B. Brun, S. Zihlmann, T. Nguyen, V. Champain, J. C. Abadillo-Uriel, B. Bertrand, H. Niebojewski, R. Maurand, Y.-M. Niquet, X. Jehl, S. D. Franceschi, and V. Schmitt, *Optimal operation of hole spin qubits* (2024), arXiv:2412.13069 [cond-mat.mes-hall].
- [53] B. Martinez, J. C. Abadillo-Uriel, E. A. Rodríguez-Mena, and Y.-M. Niquet, Hole spin manipulation in inhomogeneous and nonseparable electric fields, *Phys. Rev. B* **106**, 235426 (2022).
- [54] J. C. Abadillo-Uriel, E. A. Rodríguez-Mena, B. Martinez, and Y.-M. Niquet, Hole-spin driving by strain-induced spin-orbit interactions, *Physical Review Letters* **131**, 097002 (2023).
- [55] B. Martinez, S. de Franceschi, and Y.-M. Niquet, Mitigating variability in epitaxial-heterostructure-based spin-qubit devices by optimizing gate layout, *Phys. Rev. Appl.* **22**, 024030 (2024).
- [56] L. F. Peña, J. C. Koepke, J. H. Dycus, A. Mounce, A. D. Baczewski, N. T. Jacobson, and E. Bussmann, Modeling si/sige quantum dot variability induced by interface disorder reconstructed from multiperspective microscopy, *npj Quantum Information* **10**, 33 (2024).
- [57] R. R. Reeber and K. Wang, Thermal expansion and lattice parameters of group IV semiconductors, *Materials Chemistry and Physics* **46**, 259 (1996).
- [58] C. Corley-Wiciak, C. Richter, M. H. Zoellner, I. Zaitsev, C. L. Manganelli, E. Zatterin, T. U. Schüllli, A. A. Corley-Wiciak, J. Katzer, F. Reichmann, W. M. Klesse, N. W. Hendrickx, A. Sammak, M. Veldhorst, G. Scappucci, M. Virgilio, and G. Capellini, Nanoscale Mapping of the 3D Strain Tensor in a Germanium Quantum Well Hosting a Functional Spin Qubit Device, *ACS Applied Materials & Interfaces* **15**, 3119 (2023).
- [59] L. Massai, B. Hetényi, M. Mergenthaler, F. J. Schupp, L. Sommer, S. Paredes, S. W. Bedell, P. Harvey-Collard, G. Salis, A. Fuhrer, and N. W. Hendrickx, Impact of interface traps on charge noise and low-density transport properties in ge/sige heterostructures, *Communications Materials* **5**, 151 (2024).
- [60] J. C. Abadillo-Uriel, B. Martinez, M. Filippone, and Y.-M. Niquet, Two-body wigner molecularization in asymmetric quantum dot spin qubits, *Physical Review B* **104**, 195305 (2021).
- [61] M. J. Rodríguez, E. A. Rodríguez-Mena, A. F. Kalo, and Y.-M. Niquet, *Dressed basis sets for the modeling of exchange interactions in double quantum dots* (2025), arXiv:2504.18281 [cond-mat.mes-hall].
- [62] B. Venitucci, L. Bourdet, D. Pouzada, and Y.-M. Niquet, Electrical manipulation of semiconductor spin qubits within the g -matrix formalism, *Physical Review B* **98**, 155319 (2018).
- [63] Note that for a normal distribution, the median is equal to the mean, and the IQR is roughly 1.35 times the standard deviation.
- [64] A. C. Davison and D. V. Hinkley, *Bootstrap methods and their application*, Cambridge Series in Statistical and Probabilistic Mathematics (Cambridge University Press, 1997).
- [65] A. Crippa, R. Maurand, L. Bourdet, D. Kotekar-Patil, A. Amisse, X. Jehl, M. Sanquer, R. Laviéville, H. Bohuslavskiy, L. Hutin, S. Barraud, M. Vinet, Y.-M. Niquet, and S. De Franceschi, Electrical spin driving by g -matrix modulation in spin-orbit qubits, *Physical Review Letters* **120**, 137702 (2018).
- [66] The IQR of θ_g is 0.08° at $n_i = 10^{11} \text{ cm}^{-2}$. It reaches $\mathcal{R}(\theta_g) = 0.09$ degrees for $n_i = 10^{12} \text{ cm}^{-2}$, and it goes down to 0.03° for $n_i = 10^{10} \text{ cm}^{-2}$. Note that $\bar{\theta}_g \rightarrow 0$ when $n_i \rightarrow 0$.
- [67] L. Mauro, E. A. Rodríguez-Mena, B. Martinez, and Y.-M. Niquet, Strain engineering in Ge/Ge-Si spin-qubit heterostructures, *Phys. Rev. Appl.* **23**, 024057 (2025).
- [68] E. Marcellina, A. R. Hamilton, R. Winkler, and D. Culcer, Spin-orbit interactions in inversion-asymmetric two-dimensional hole systems: A variational analysis, *Physical Review B* **95**, 075305 (2017).
- [69] L. A. Terrazos, E. Marcellina, Z. Wang, S. N. Copper-Smith, M. Friesen, A. R. Hamilton, X. Hu, B. Koiller, A. L. Saraiva, D. Culcer, and R. B. Capaz, Theory of hole-spin qubits in strained germanium quantum dots, *Physical Review B* **103**, 125201 (2021).
- [70] S. Bosco, M. Benito, C. Adelsberger, and D. Loss, Squeezed hole spin qubits in ge quantum dots with ultrafast gates at low power, *Physical Review B* **104**, 115425 (2021).
- [71] If the electric drive only gives rise to conventional g -TMR, $\hat{g}' = \text{diag}(g'_1, g'_2, g'_3)$. If $\mathbf{B} = (B_1, B_2, 0)$, then $\|\mathbf{g}\mathbf{B} \times \mathbf{g}'\mathbf{B}\| = |g_1 g'_2 B_1 B_2 - g_2 g'_1 B_2 B_1|$. In a circular QD $g_1 = g_2$; and if it is perfectly centered under the C gate then $g'_1 = g'_2$. Therefore, the in-plane Rabi frequency is zero. If the QD is not perfectly circular and/or not perfectly centered under the C gate, f_R is only zero when \mathbf{B} is parallel to the axes of \mathbf{g}_1 or \mathbf{g}_2 .
- [72] We have restricted the contributions to the C and side gates, as the contribution from the second nearest neighbors is found to be negligible.
- [73] M. Veldhorst, H. G. J. Eenink, C. H. Yang, and A. S. Dzurak, Silicon CMOS architecture for a spin-based quantum computer, *Nature Communications* **8**, 1766 (2017).
- [74] We emphasize that U may also be tuned with V_C , and that $\mathcal{R}(\mu)$ shows only a weak dependence on gate voltage (see Appendix C).

- [75] D. Bauza, Extraction of Si-SiO₂ interface trap densities in MOS structures with ultrathin oxides, *IEEE Electron Device Letters* **23**, 658 (2002).
- [76] L. Brunet, X. Garros, F. Andrieu, G. Reibold, E. Vincent, A. Bravaix, and F. Boulanger, New method to extract interface states density at the back and the front gate interfaces of FDSOI transistors from CV-GV measurements, in *2009 IEEE International SOI Conference* (2009) p. 1.
- [77] L. Pirro, I. Ionica, G. Ghibaud, X. Mescot, L. Faraone, and S. Cristoloveanu, Interface trap density evaluation on bare silicon-on-insulator wafers using the quasi-static capacitance technique, *Journal of Applied Physics* **119**, 175702 (2016).
- [78] M. L. Vermeer, R. J. E. Hueting, L. Pirro, J. Hoentschel, and J. Schmitz, Interface states characterization of UTB SOI MOSFETs from the subthreshold current, *IEEE Transactions on Electron Devices* **68**, 497 (2021).
- [79] V. P. Michal, B. Venitucci, and Y.-M. Niquet, Longitudinal and transverse electric field manipulation of hole spin-orbit qubits in one-dimensional channels, *Physical Review B* **103**, 045305 (2021).
- [80] D. Costa, L. E. A. Stehouwer, Y. Huang, S. Martí-Sánchez, D. Degli Esposti, J. Arbiol, and G. Scappucci, Reducing disorder in Ge quantum wells by using thick SiGe barriers, *Applied Physics Letters* **125**, 222104 (2024).